JOURNAL OF GEOPHYSICAL RESEARCH, VOL. 112, E05016, doi:10.1029/2006JE002815, 2007

Water vapor diffusion in Mars subsurface environments

Troy L. Hudson,[1] Oded Aharonson,[1] Norbert Schorghofer,[1,2] Crofton B. Farmer,[3] Michael H. Hecht,[3] and Nathan T. Bridges[3]

Received 18 August 2006; revised 29 November 2006; accepted 1 February 2007; published 31 May 2007.

[1] The diffusion coefficient of water vapor in unconsolidated porous media is measured for various soil simulants at Mars-like pressures and subzero temperatures. An experimental chamber which simultaneously reproduces a low-pressure, low-temperature, and low-humidity environment is used to monitor water flux from an ice source through a porous diffusion barrier. Experiments are performed on four types of simulants: 40–70 μm glass beads, sintered glass filter disks, 1–3 μm dust (both loose and packed), and JSC Mars–1. A theoretical framework is presented that applies to environments that are not necessarily isothermal or isobaric. For most of our samples, we find diffusion coefficients in the range of 2.8 to 5.4 $cm^2\ s^{-1}$ at 600 Pascal and 260 K. This range becomes 1.9–4.7 $cm^2\ s^{-1}$ when extrapolated to a Mars-like temperature of 200 K. Our preferred value for JSC Mars–1 at 600 Pa and 200 K is $3.7 \pm 0.5\ cm^2\ s^{-1}$. The tortuosities of the glass beads is about 1.8. Packed dust displays a lower mean diffusion coefficient of $0.38 \pm 0.26\ cm^2\ s^{-1}$, which can be attributed to transition to the Knudsen regime where molecular collisions with the pore walls dominate. Values for the diffusion coefficient and the variation of the diffusion coefficient with pressure are well matched by existing models. The survival of shallow subsurface ice on Mars and the providence of diffusion barriers are considered in light of these measurements.

Citation: Hudson, T. L., O. Aharonson, N. Schorghofer, C. B. Farmer, M. H. Hecht, and N. T. Bridges (2007), Water vapor diffusion in Mars subsurface environments, *J. Geophys. Res.*, *112*, E05016, doi:10.1029/2006JE002815.

1. Introduction and Literature Review

[2] Large amounts of subsurface ice exist on Mars, both at present and during past periods [*Carr*, 1996; *Boynton et al.*, 2002]. The rate of water vapor diffusion through the regolith determines how long ice can survive in the subsurface when exposed to a drier atmosphere. It also determines how fast the regolith can be recharged with atmospherically derived vapor [*Mellon and Jakosky*, 1993]. Vapor diffusion in soils is further relevant to records of climate change on Earth, where ground ice has survived for extensive time periods [*Sugden et al.*, 1995; *Hindmarsh et al.*, 1998]. Constraining these rates motivate the study of the diffusion of water vapor in a planetary subsurface.

[3] An experimental facility has been constructed to create a controlled environment which approximates the conditions appropriate to examining the evolution and transport of water in the upper regolith of Mars. Section 2 elaborates on the theory of diffusion used to interpret the results. Section 3 describes the experimental methods and materials used and section 4 details the data analysis. Section 5 summarizes the results for the various simulants and conditions studied. These results and their implications to studies of Mars and other buried ice systems are discussed in section 6.

[4] Numerical values of the diffusion coefficient for water vapor transport through the Martian regolith have been used by a number of previous investigators as a parameter in models of subsurface H_2O communication with the atmosphere and ice cap systems. The following briefly summarizes the values used in a number of important papers which consider diffusion on Mars.

[5] Many of the papers listed below calculate diffusion coefficients from the kinetic theory of gases as applied to porous media. All such methods require additional input parameters describing the geometry of the pore space. Porosity, or void volume, may be calculated from particle size distributions and shapes or measured directly for real samples. Another parameter describing the degree of interconnectivity and convolution of the void space, called tortuosity, cannot be measured directly. Even for model pore spaces, the value of this dimensionless number is model dependent and intractable to calculate in all but the most simple cases. There is also no robust relationship between porosity and tortuosity that holds for a wide variety of particle shapes and sizes. The ratio of porosity to tortuosity parameterizes the change in diffusion coefficient

[1] Division of Geological and Planetary Sciences, California Institute of Technology, Pasadena, California, USA.
[2] Now at Institute for Astronomy, University of Hawaii, Honolulu, Hawaii, USA.
[3] Jet Propulsion Laboratory, California Institute of Technology, Pasadena, California, USA.

0148-0227/07/2006JE002815$09.00

from free-gas to porous-media conditions and is called the obstruction factor. The value of tortuosity is usually obtained from experiment by measuring porosity and diffusivity.

[6] In a seminal paper, *Smoluchowski* [1968] calculates diffusion coefficients for a range of particle sizes and porosities from the kinetic theory of gases as presented by *Kennard* [1938] and *Evans et al.* [1961]. He presents a range of values between 4×10^{-4} and 12 $cm^2\ s^{-1}$, but the lower end of this range is for 1–10% porosities and particle diameters less than 10 μm. For porosities of 50–80% and 10–200 μm sized particles, values between 0.7 and 11 $cm^2\ s^{-1}$ are obtained. Smoluchowski gives no reference for tortuosity values but presents values of 1, 5, and 10, for 80%, 50%, and lower porosities, respectively.

[7] *Flasar and Goody* [1976] directly reference measurements of gas diffusion in porous media. The works cited by them include *Currie* [1960], who performed experiments on hydrogen diffusion in air at STP and considered diffusion in dry granular materials, and also *Papendick and Runkles* [1965] whose work considered oxygen diffusion in porous media at STP. Both of these works present factors relating free-gas diffusion to porous media diffusion for a variety of materials. Flasar and Goody use these to determine a range of porous-media diffusion coefficients for the surface of Mars of 0.4–13.6 $cm^2\ s^{-1}$ at 610 Pa and 210 K. The upper limit they give is the temperature- and pressure-extrapolated value of free-gas diffusion given by Boyton and Brattain in the work by *Washburn et al.* [2003] (but see section 2.2). A real porous medium would have an obstruction factor of less than unity, and so the diffusion coefficient should be smaller than this limit.

[8] *Farmer* [1976] cites both *Smoluchowski* [1968] and *Evans et al.* [1961] and quotes Smoluchowski's values directly. *Jakosky* [1983] references *Flasar and Goody* [1976] but gives a slightly modified range of 0.3–10 $cm^2\ s^{-1}$. He then claims that his model, with a regolith diffusivity of 1.0 $cm^2\ s^{-1}$, matches the observed amplitude of Martian seasonal variation in atmospheric water content at 25°N latitude, and that a range of 1.0–3.0 $cm^2\ s^{-1}$ is likely appropriate for Mars.

[9] The problem of diffusion on Mars was examined in great detail by *Clifford and Hillel* [1983], who cite measurements of diffusion in porous media, all of which were performed at 25–30°C. Most involved the diffusion of H_2 or He, and many were performed at pressures of 1 atmosphere or higher. Their derivation from kinetic theory computes values for diffusivity given only a pore size distribution and a value for tortuosity.

[10] *Fanale et al.* [1986] and *Zent et al.* [1986], in tandem papers, perform their own calculations to derive diffusivity from gas kinetics and reference *Smoluchowski* [1968] for values of tortuosity. They use a porosity of 50% for all cases and a tortuosity of 5. For a pressure of 610 Pa and a temperature of 210 K, their expression gives a free-gas diffusivity of 13.2 $cm^2\ s^{-1}$ and a porous medium diffusivity of 0.44 $cm^2\ s^{-1}$. These values are essentially the same as the limits given by *Flasar and Goody* [1976].

[11] *Fanale et al.* [1986] estimates a Knudsen diffusion coefficient of 0.02–0.22 $cm^2\ s^{-1}$ for pore radii from 1 to 10 μm. A later paper by *Clifford and Hillel* [1986] focused on Knudsen diffusion in the Mars regolith.

[12] *Mellon and Jakosky* [1993] present a diffusive model for the regolith. This work includes a detailed derivation of the porous media diffusion coefficient similar to *Clifford and Hillel* [1983], but uses collision integrals to calculate free-gas diffusion coefficients, while Clifford and Hillel cite *Wallace and Sagan* [1979]. For a pressure of 600 Pascal, a temperature of 200 K, and a pore radius of 1–10 μm, the expression of Mellon and Jakosky gives an effective diffusion coefficient of 2–10 $cm^2\ s^{-1}$.

[13] We are aware of no direct measurements of the diffusion of any gases in porous media at conditions of low temperature and Mars-surface pressures in the literature. Experiments referenced in the above papers were performed above freezing and at high (relative to Mars) pressures. Additionally, there are very few measurements of the diffusion in porous media of the condensible and highly absorptive gas water vapor. The measurements of free-gas diffusion of H_2O in CO_2 have been done at conditions other than those appropriate Mars' surface and extrapolated in temperature and pressure. These data are reviewed in greater detail in section 2.2.

2. Theoretical Framework

[14] Here we develop expressions for vapor transport in a sublimation environment where temperature and pressure can change with time and space. Throughout this paper, subscript 1 refers to H_2O and subscript 2 to the carrier gas, usually CO_2. For example, p_1 is the partial pressure of H_2O and ρ_1 the density of water vapor. The total pressure is denoted by $p_0 = p_1 + p_2$ and the total mass density by $\rho_0 = \rho_1 + \rho_2$. A script $\mathcal{D}$ refers to free-gas diffusion coefficients while roman italic D refers to diffusion in a porous medium.

2.1. Vapor Transport

[15] Diffusion of mass is due to differences in concentration, temperature, and pressure [*Reid et al.*, 1987]. The general expression for diffusive flux of one dilute gas (species 1) in another (species 2) at low velocities is [*Landau and Lifshitz*, 1987, chaps. 57 and 58]

$$J_{\mathrm{Diff}} = -\rho_0 \left[\mathcal{D}_{12} \frac{\partial}{\partial z} \frac{\rho_1}{\rho_0} + \frac{\mathcal{D}_T}{T} \frac{\partial T}{\partial z} + \frac{\mathcal{D}_p}{p_0} \frac{\partial p_0}{\partial z} \right], \tag{1}$$

where J_{Diff} is the diffusive mass flux of gas 1, $\mathcal{D}_{12}$ the mutual diffusion coefficient, $\mathcal{D}_T$ the coefficient for "thermodiffusion", T the temperature, and $\mathcal{D}_p$ the coefficient of "barodiffusion". Thermodiffusion and barodiffusion are usually small compared with concentration diffusion (see sections 2.5 and 2.6).

[16] Equation (1) holds in a reference frame where the center of mass velocity of the gas mixture is zero. In an environment where temperature and total pressure change little, and the vapor concentration is low, the concentration diffusion J_{Diff} would be simply described by

$$J_{\mathrm{Diff}} = -\mathcal{D}_{12} \frac{\partial \rho_1}{\partial z}. \tag{2}$$

For a detailed discussion of reference frames and nonisothermal diffusion laws, see *Cunningham and Williams* [1980].

Table 1. Model Parameters for the Mutual Diffusion Coefficient[a]

Parameter	Value	Reference
σ^{hes} (CO_2, N_2)	4.63, 3.76 Å	*Chapman and Cowling* [1970]
σ^{hes} (H_2O)	2.7 Å	*Schwertz and Brow* [1951]
σ^{LJ} (H_2O, CO_2, N_2)	2.641, 3.941, 3.798 Å	*Reid et al.* [1987]
ε/k (H_2O, CO_2, N_2)	809.1, 195.2, 71.4 K	*Reid et al.* [1987]

[a]Parameters are as follows: σ^{hes} = molecular radius of hard elastic spheres, σ^{LJ} and ε/k are parameters of the Lennard-Jones potential. The collision integral for the Lennard-Jones potential can be expressed as $\Omega_{12} = A(T^*)^{-B} + Ce^{-DT^*} + Ee^{-FT^*} + Ge^{-HT^*}$. Values for the constants A, B, C, D, E, F, G, and H are given by *Neufeld et al.* [1972] and *Reid et al.* [1987]. The dimensionless temperature T^* is given by $T^* = kT/\varepsilon_{12}$ and the molecule specific parameter ε is computed for a gas pair by $\varepsilon_{12} = \sqrt{\varepsilon_1 \varepsilon_2}$.

[17] Mass transfer of a gas results not only from diffusion but also from advection, where a difference in pressure causes the gas to move as a whole. The vertical velocity of gas w is given by Darcy's law,

$$w = -\frac{\kappa}{\mu}\frac{\partial p_0}{\partial z}, \tag{3}$$

where κ is the intrinsic permeability of the porous medium and μ the dynamic viscosity of the gas. The total mass flux is the sum of diffusive and advective transport,

$$J_1 = J_{\mathrm{Diff}} + J_{\mathrm{Adv}} = J_{\mathrm{Diff}} + w\rho_1, \tag{4}$$

where $J_{\mathrm{Adv}} = w\rho_1$.

[18] The porosity ϕ of a porous medium restricts the cross sectional area available for transport. A second factor called tortuosity τ accounts for the increase in path length which the molecules must follow. The diffusion coefficient in a porous medium can be written as [*Mason and Malinauskas*, 1983]

$$D = \frac{\phi}{\tau}\mathcal{D}_{12}. \tag{5}$$

[19] The ratio ϕ/τ is also called the "obstruction factor." In principle, this reduction in diffusivity can be obtained theoretically from the void space geometry. In practice, the void space geometry is seldom known, even for terrestrial soils in a laboratory environment.

[20] In a porous medium, equation (2) is replaced by

$$J_{\mathrm{Diff}} = -D\frac{\partial \rho_1}{\partial z}. \tag{6}$$

2.2. Diffusion Coefficient

[21] The coefficient of diffusion is the product of mean velocity and mean free path, with a prefactor that can be temperature dependent. The mean velocity depends only on temperature. The mean free path is inversely proportional to the density of the gas. Thus a thinner atmosphere has a higher diffusivity. The diffusivity of an unconfined gas at rest, in which molecules diffuse through an interstitial gas, forms the basis for understanding the diffusivity of a porous regolith.

[22] Theoretical expressions can be obtained for the diffusion coefficient, $\mathcal{D}_{12}$, in a dilute gas at rest consisting of vapor species 1 and 2. The coefficient of self-diffusion, $\mathcal{D}_{11}$, is not measured in our experiments.

[23] The coefficient of diffusion in a binary mixture of rigid elastic spherical molecules is, to first order in the density of the diffusing species [*Chapman and Cowling*, 1970],

$$\mathcal{D}_{12} = \frac{3}{8n_0\sigma_{12}^2}\sqrt{\frac{kT}{2\pi}\left(\frac{1}{m_1}+\frac{1}{m_2}\right)}. \tag{7}$$

The number density n_0 is obtained from the ideal gas law, $n_0 = p_0/kT$, $\pi\sigma_{12}^2$ is the scattering cross section, k is the Boltzmann constant, and m_1 and m_2 are the molecular masses.

[24] The parameter σ_{12} is computed by averaging the molecular radii of each species, $\sigma_{12} = (\sigma_1 + \sigma_2)/2$. The cross section for individual molecules can be determined from viscosity measurements of pure gases. *Chapman and Cowling* [1970] report molecular radii for CO_2 and N_2. *Schwertz and Brow* [1951] calculate a molecular radius for H_2O from the molecular volume of the liquid. The values are listed in Table 1.

[25] For intermolecular forces other than a model of rigid elastic spheres, a temperature-dependent prefactor is introduced via the collision integral $\Omega_{12}(T)$ [*Mason and Malinauskas*, 1983; *Reid et al.*, 1987],

$$\mathcal{D}_{12} = \frac{3}{8n_0\sigma_{12}^2}\sqrt{\frac{kT}{2\pi}\left(\frac{1}{m_1}+\frac{1}{m_2}\right)}\frac{1}{\Omega_{12}(T)}. \tag{8}$$

[26] The length parameter σ_{12} now depends on the intermolecular force law and its value is not the same as for the rigid elastic spherical molecules. For a Lennard-Jones potential, the function $\Omega_{12}(T)$ and parameters for H_2O, CO_2, and N_2 are given in Table 1.

[27] For an ideal gas of hard elastic spheres, the diffusion coefficient depends on temperature as $T^{3/2}$, as can be seen from equation (7). For other intermolecular potentials, the temperature dependence is described by equation (8), and can be shown to have an exponent between 0 and 2. The diffusion coefficient is inversely proportional to pressure for any intermolecular potential.

[28] Equation (8) is a first-order expansion derived from Chapman-Enskog theory. To lowest order, the diffusion coefficient does not depend on the relative concentration of the two gases n_1/n_2 but only on the total number density $n_0 = n_1 + n_2$ and on the temperature. Hence the diffusion coefficient is symmetric, $\mathcal{D}_{12} = \mathcal{D}_{21}$.

[29] The second-order approximation of the diffusion coefficient introduces a dependence on n_1/n_2 [*Chapman and Cowling*, 1970]. For a hard sphere model and low concentrations of species 1 ($n_1 \ll n_2$), the diffusion coefficient is increased by a factor of

$$\frac{1}{1 - m_1^2/\left(13m_1^2 + 30m_2^2 + 16m_1m_2\right)}.$$

For low H_2O concentration in a CO_2 or N_2 atmosphere, this correction is <1%. The maximum correction for any mixing

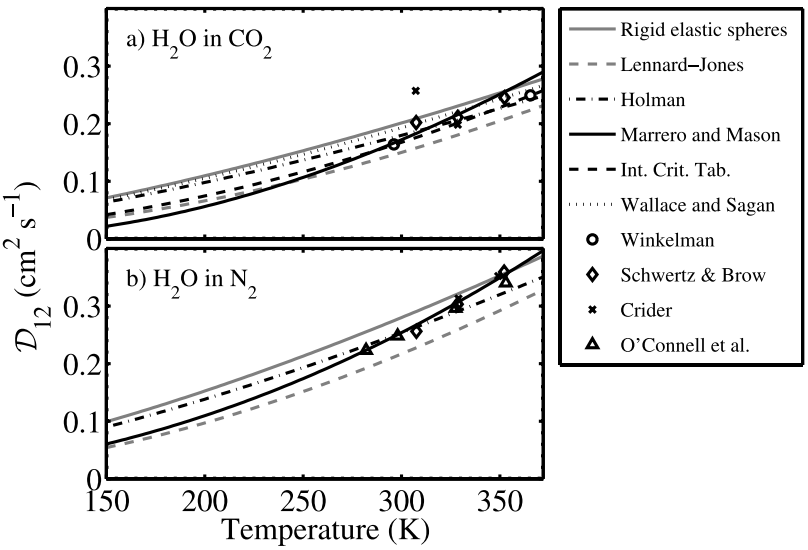

Figure 1. Theoretical and measured diffusion coefficients for H_2O in (a) CO_2 and (b) N_2 as a function of temperature at 1013 mbar. Grey lines are theoretical formulae with model parameters, black lines indicate fits to measured values, and individual markers indicate specific measured values.

ratio for H_2O–CO_2 is 4%, and for H_2O–N_2 it is 2%, both occurring as $n_2 \rightarrow 0$. Hence the dependence of the diffusion coefficient on the proportions of the mixture can be neglected in comparison to other uncertainties.

[30] *Holman* [1997] gives a semiempirical equation by *Gilliland et al.* [1974]

$$\mathcal{D}_{12} = 435.7 \text{ cm}^2 \text{ s}^{-1} \frac{T^{3/2}}{p_0\left(V_1^{1/3} + V_2^{1/3}\right)^2} \sqrt{\frac{1}{M_1} + \frac{1}{M_2}},$$

where T is in Kelvin, p is in pascals, V_1 and V_2 are molecular volumes of 1 and 2, and M_1 and M_2 are their molar weights. Holman cautions that this expression is useful for various mixtures, but should not be used in place of experimental values of $\mathcal{D}_{12}$ when available.

[31] The coefficient of mutual diffusion $\mathcal{D}_{12}$ has been directly measured from evaporation rates of water into pure gases. Measurements for H_2O–CO_2 are reported or compiled by *Guglielmo* [1882], *Winkelmann* [1884a, 1884b, 1889], *Trautz and Müller* [1935a, 1935b] *Schwertz and Brow* [1951], *Rossie* [1953], and *Crider* [1956] in the temperature range 291–373 K at atmospheric pressure. *Nagata and Hasegawa* [1970] use gas chromatography to determine the diffusivity at 394 K and higher temperatures. The International Critical Tables [*Washburn et al.*, 2003] list $\mathcal{D}_{H_2O\cdot CO_2} = (0.1387 \text{ cm}^2 \text{ s}^{-1})(T/T_0)^2 (p_{ref}/p)$, citing the experiments by Guglielmo and Winkelmann. The comprehensive review of gaseous diffusion coefficients by *Marrero and Mason* [1972] recommends $\mathcal{D}_{H_2O\cdot CO_2} = (9.24 \times 10^{-5} \text{ cm}^2 \text{ s}^{-1}) T^{3/2} \exp(-307.9/T)(p_{ref}/p)$ for T in the range 296–1640 K. A diffusivity scaling often cited in the context of Mars studies is from *Wallace and Sagan* [1979], who use a prefactor determined from *Schwertz and Brow* [1951] to write $\mathcal{D}_{H_2O\cdot CO_2} = (0.1654 \text{ cm}^2 \text{ s}^{-1})(T/T_0)^{3/2}(p_{ref}/p_0)$. In all cases, $p_{ref} = 1013$ mbar and $T_0 = 273.15$ K.

[32] Measurements for H_2O–N_2 are available from *Hippenmeyer* [1949], *Schwertz and Brow* [1951], *Bose and Chakraborty* [1955–1956], *Crider* [1956], *Nelson* [1956], and *O'Connell et al.* [1969] in the range 273–373 K. *Marrero and Mason* [1972] recommend $\mathcal{D}_{H_2O\cdot N_2} = (1.87 \times 10^{-6} \text{ cm}^2 \text{ s}^{-1}) \times T^{2.072} (p_{ref}/p_0)$ in the temperature range 282–373 K.

[33] Figure 1 shows theoretical and experimental values of the mutual diffusion coefficient as a function of temperature. The empirical fits from *Marrero and Mason* [1972] and the International Critical Tables are based on measurements at high temperature and may not provide accurate results when extrapolated to low temperatures. The empirical fits, the theoretical formula for a Lennard-Jones potential, and the theoretical formula for hard elastic spherical molecules predict slightly different temperature dependencies. Measurement errors and uncertainties in cross sections introduce additional deviations that limit the accuracy to which diffusion coefficients can be computed for a free gas.

[34] The Martian atmosphere consists of 95% CO_2, the next most abundant gases being nitrogen and argon. The fraction of gases other than CO_2 is small enough to be ignored and we consider a pure CO_2 atmosphere. According to the elastic hard sphere model, equation (7), the diffusion coefficient in CO_2 is smaller than in N_2 at the same pressure and temperature by a factor of

$$\frac{\mathcal{D}_{H_2O\cdot CO_2}}{\mathcal{D}_{H_2O\cdot N_2}} = \frac{\sigma^2_{H_2O\cdot N_2}}{\sigma^2_{H_2O\cdot CO_2}} \frac{\sqrt{1/18 + 1/44}}{\sqrt{1/18 + 1/28}} \approx 0.72. \quad (9)$$

Assuming a Lennard-Jones potential, this ratio would be 0.68–0.69 in the temperature range 150–293 K.

2.3. Mean Free Path and Knudsen Diffusion

[35] The mean free path for species 1, diffusing in a gas composed of species 1 and 2, is [*Chapman and Cowling*, 1970]

$$\lambda_1 = \frac{1}{n_1 \pi \sigma_{i1}^2 \sqrt{2} + n_2 \pi \sigma_{i2}^2 \sqrt{1 + m_1/m_2}}. \quad (10)$$

[36] When only one gas is present, the familiar formula $\lambda_1 = 1/(\sqrt{2}\, n\pi\sigma^2)$ is recovered. When $n_1 \ll n_2$, the first term in the denominator, resulting from like-molecule collisions, is negligible. With this expression, the mean free path of H_2O in a dry CO_2 atmosphere at 600 Pa and 200 K is $\lambda_1 \approx 9\ \mu$m. The mean free path of H_2O in a dry N_2 atmosphere is longer than in a dry CO_2 atmosphere at the same pressure and temperature by a factor of 1.2.

[37] In a porous solid with interconnected pathways, a gas molecule may collide with another molecule or with the pore walls. When the gas pressure is high, molecule-molecule collisions dominate and the system is said to be in the normal or Fickian regime.

[38] At low pressure, collisions are dominantly between molecules and the walls, and the free path is restricted by the geometry of the void space. In this regime, termed Knudsen diffusion, the presence of other gases no longer affects the transport, and the flux depends only on the density gradient of the species of interest (water in this study) and can be written as [*Mason and Malinauskas*, 1983]

$$J_1 = -D_K \frac{\partial \rho_1}{\partial z}. \tag{11}$$

[39] As for Fickian diffusion, the Knudsen diffusion coefficient D_K is proportional to the mean velocity. For example, in a long, straight, circular capillary of radius $r \ll \lambda_1$, the diffusion coefficient at low pressure is $D_K = (2/3)\bar{v}_1 r$, where the mean velocity is $\bar{v}_1 = \sqrt{8kT/\pi m_1}$ [*Mason and Malinauskas*, 1983; *Clifford and Hillel*, 1986].

[40] *Evans et al.* [1961] give an expression for D_K in materials with interconnected, convoluted pore spaces

$$D_K = \frac{4}{3}\bar{v}_1 K_0, \tag{12}$$

where K_0 is a structural parameter (with dimensions of length) accounting for both pore geometry and the scattering of the diffusing molecules off the pore walls. They give an expression for K_0

$$\frac{1}{K_0} = \frac{128}{9} n_d \frac{\tau}{\phi} r^2 \left(1 + \frac{1}{8}\pi a_1\right), \tag{13}$$

where n_d is the number density of "dust" particles (meaning the porous medium). Here r is the particle size in the dusty gas model (which may be an average of a particle size distribution), and a_1 is the fraction of molecules that are both scattered diffusely and have their speeds thermalized to a Maxwellian distribution. *Evans et al.* [1961] suggest that a_1 is 1 for most gases. In the case of spherical particles with an average radius $\bar{r}$, n_d can be estimated as $(3/4)(1-\phi)/\pi\,\bar{r}^3$, giving

$$D_K = \frac{\pi}{8+\pi}\frac{\phi}{1-\phi}\frac{\bar{v}_1 \bar{r}}{\tau}. \tag{14}$$

These expressions show that D_K is independent of pressure and changes as $T^{1/2}$ with temperature.

[41] At intermediate pressures, both collisions with pore walls and with other molecules occur with significant frequency. This "transition region" is defined by the ratio of pore size to mean free path r/λ_1. In the Knudsen regime r/λ_1 is much smaller than 1 and in the Fickian regime r/λ_1 is much greater than 1. Equations (2) and (11) can be combined by summing their contributions to $\partial\rho_1/\partial z$. Neglecting advection in (2) and rewriting $\mathcal{D}_{12}$ as the Fickian diffusion coefficient in a porous medium D_F, we obtain

$$\frac{\partial \rho_1}{\partial z} = -J_1\left(\frac{1}{D_F} + \frac{1}{D_K}\right). \tag{15}$$

Thus the combined or effective diffusion coefficient may be written

$$\frac{1}{D} = \frac{1}{D_F} + \frac{1}{D_K}. \tag{16}$$

This is known as the Bosanquet relation and was discussed by *Pollard and Present* [1948] and more recently described by *Mason and Malinauskas* [1983] in the context of gas diffusion through porous media.

2.4. Advection

[42] Diffusion describes the relative motion of gases, while advection represents the bulk motion of the gas. For sublimation from an impermeable layer, the lower boundary condition is $J_2 = 0$. The total mass flux, however, is not zero because the ice is a source of vapor, $J_1 \neq 0$. Mass conservation for species 1 and 2 requires [*Landau and Lifshitz*, 1987]

$$J_1 = -\mathcal{D}_{12}\rho_0 \frac{\partial}{\partial z}\frac{\rho_1}{\rho_0} + w\rho_1 \tag{17}$$

$$J_2 = -\mathcal{D}_{12}\rho_0 \frac{\partial}{\partial z}\frac{\rho_2}{\rho_0} + w\rho_2 = 0. \tag{18}$$

[43] The ratio of advective to diffusive flux can be obtained by dividing the second term of the first equation by the first term. Solving the second equation for w and substituting, we obtain

$$\frac{J_{\mathrm{Adv}}}{J_{\mathrm{Diff}}} = \frac{c(z)}{1-c(z)}. \tag{19}$$

The mass concentration of H_2O is denoted by $c = \rho_1/\rho_0$. The total flux is given by

$$J_1 = -\mathcal{D}_{12}\rho_0 \frac{1}{1-c}\frac{\partial c}{\partial z}. \tag{20}$$

[44] When the CO_2 column is at rest and H_2O vapor moves outward, the gas mixture as a whole effectively moves outward, and there must always be a pressure difference Δp_0 across the sample that drives this advective

flow. On the other hand, the pressure difference can never exceed the saturation vapor pressure over ice. The factor of $1/(1 - c)$ is an approximate estimate of the error due to advective flux counted as diffusive.

[45] The saturated vapor pressure over ice at 260 K is 195.8 Pa. In 600 Pa of CO_2, this gives a large advective correction factor, $1/(1 - c)$, of 1.32. However, at the upper sample surface the partial pressure of water is significantly lower and the correction factor is found to be 1.01–1.07 at this location in our experiments. The error thus introduced by the average value of c is on the order of 10%. It will be shown that this error is of the same order as the systematic scatter in our experimental determinations of D.

[46] For small c, the advective contribution disappears, $J_1 = J_{\mathrm{Diff}}$, and the pressure difference also becomes negligible. The concentration of water vapor is limited when saturation vapor pressures are low. In our experiment, a compromise is reached between low-temperature conditions with small advection contributions and higher temperature conditions which allow more rapid sample turnover.

[47] On Mars, pressure differences, and therefore advection, can result from winds or thermal expansion. A temperature increase by 30% leads to a thermal expansion by 30% over a thermal skin depth, which is on the order of 1 m for the annual cycle and 3 cm for the diurnal cycle. The expansion thus corresponds to an airflow of 30 cm per year for the annual cycle and 1 cm per sol diurnally. The velocity of water vapor due to concentration differences is the diffusion coefficient divided by depth. For example, for $D = 10\ \mathrm{cm^2\ s^{-1}}$ and ice buried 100 cm, the diffusive flux is 0.01 cm/s or 9 m per sol, many orders of magnitude faster than thermal expansion.

[48] Most of our experiments take place at a total chamber pressure of ~600 Pa. At the ice surface, there is a pressure contribution both from the CO_2 in the chamber and the saturation pressure of H_2O. Assuming the pressure difference across the sample equals the saturation vapor pressure, we can set a lower bound on permeability. From equations (3), (4), and (19),

$$J_1 \Delta z = -\rho_0 \frac{\kappa}{\mu} \Delta p_0. \tag{21}$$

The viscosity of CO_2 and N_2 at 200 K and 1 bar pressure are 1.00×10^{-5} Pa s and 1.29×10^{-5} Pa s, respectively [*Lide*, 2003]. Using measured values of $J_1 \approx 10^{-5}$ kg m^{-2} s^{-1}, $\Delta z = 0.05$ m, and $\rho_0 \approx 0.01$ kg m^{-3} from one of our experiments on 40–70 μm glass beads, the minimum permeability is $\kappa = 3 \times 10^{-12}$ m^2 or 3 darcy. This is similar to permeability values measured for grains tens of microns in size, where $\kappa \sim 10^{-12}$ m^2 [*Freeze and Cheng*, 1979; *deWiest*, 1969].

2.5. Thermodiffusion

[49] In a system without concentration gradients, vapor still diffuses due to differences in temperature [*Grew and Ibbs*, 1952]. This is known as "thermal diffusion" or "thermodiffusion". The inverse effect, where the diffusion of one gas in another results in the establishment of a transient temperature gradient is known as the "diffusion thermoeffect". The liquid analog to gaseous thermodiffusion is known as the "Soret effect" [*Grew and Ibbs*, 1952]. *Chapman and Cowling* [1970] provide a first-order expression for the thermodiffusion ratio k_T,

$$k_T = \frac{\mathcal{D}_T}{\mathcal{D}_{12}} = 5(C-1)\frac{s_1 \frac{n_1}{n_1+n_2} - s_2 \frac{n_2}{n_1+n_2}}{Q_1 \frac{n_1}{n_2} + Q_2 \frac{n_2}{n_1} + Q_{12}}, \tag{22}$$

where

$$s_1 = m_1^2 E_1 - 3m_2(m_2 - m_1) + 4m_1 m_2 A$$

$$Q_1 = \frac{m_1}{m_1 + m_2} E_1 \left[6m_2^2 + (5 - 4B)m_1^2 + 8m_1 m_2 A\right]$$

$$Q_{12} = 3\left(m_1^2 - m_2^2\right) + 4m_1 m_2 A(11 - 4B) + 2m_1 m_2 E_1 E_2.$$

Analogous expressions hold for s_2 and Q_2, with interchanged indices. The thermodiffusion coefficient can be positive or negative and vanishes for low concentrations. The parameters A, B, C, E_1, and E_2 depend on the intermolecular forces. For a model of rigid elastic spherical molecules, $A = 2/5$, $B = 3/5$, $C = 6/5$, and $E_1 = (2/5m_1)\sqrt{2/m_2}\ (m_1 + m_2)^{3/2}\ \sigma_{11}^2/\sigma_{12}^2$. In the elastic hard sphere model, k_T is independent of temperature and pressure, but it does depend on the proportions of the mixture n_1/n_2 [*Chapman and Cowling*, 1970].

[50] It is conventional to introduce the thermal diffusion factor $\alpha_T = k_T\, n_0^2/(n_1\, n_2)$, which no longer vanishes for low concentrations. Using the formulae above, this factor is at most $\alpha_T \approx 0.8$ for H_2O–CO_2. For H_2O–N_2, the maximum α_T is less than 0.4. The theoretical value of the thermodiffusion ratio is thought to be larger for elastic spheres than for other models of intermolecular forces [*Chapman and Cowling*, 1970]. From equation (1), we see that thermodiffusion is reduced relative to concentration diffusion by a factor $k_T\,(\Delta T/T)/\Delta\,(\rho_1/\rho_0)$. Assuming $n_1 \ll n_2$ and $\Delta\, n_2/n_2 \ll \Delta n_1/n_1$, this factor is approximately $\alpha_T\,(m_2/m_1)\,(\Delta T/T)\,p_1/\Delta p_1$. For a typical experiment $\Delta T/T$ 0.01 and $\Delta p_1/p_1 \approx 0.5$, and thermodiffusion is smaller than concentration diffusion by a factor of $0.4 \times 0.01 \times 0.5 \times 44/18 = 0.005$ or less and therefore negligible in our measurements. On Mars, a diurnal temperature amplitude of 30 K around a mean temperature of 210 K has $\Delta T/T \sim 0.14$. It is conceivable that thermodiffusion contributes noticeably to vapor transport on Mars, but concentration diffusion still dominates.

2.6. Barodiffusion

[51] "Pressure diffusion" or "barodiffusion" is the relative diffusion of molecular species due to gradients in total pressure. *Landau and Lifshitz* [1987] and *Cunningham and Williams* [1980] provide an expression for the barodiffusion coefficient in a mixture of two ideal gases:

$$k_p = \frac{\mathcal{D}_p}{\mathcal{D}_{12}} = (m_2 - m_1)c(1-c)\left(\frac{1-c}{m_2} + \frac{c}{m_1}\right). \tag{23}$$

[52] In a single fluid there is no barodiffusion phenomenon and the coefficient vanishes. For a mixture, the coefficient can be positive or negative. Heavier molecules tend to go to regions of higher pressure. According to equation (1), barodiffusion is smaller than concentration

diffusion by a factor of $k_p(\Delta p_0/p_0)/\Delta c$. If we assume $\Delta c \approx c \ll 1$ and use equation (23), this factor is about $0.4\Delta p_0/p_0$ in an N_2 atmosphere and $0.6\Delta p_0/p_0$ in a CO_2 atmosphere. Barodiffusion is negligible when $\Delta p_0/p_0 \ll 1$.

[53] Most of our experiments take place at a total chamber pressure of ~600 Pa. At the ice surface, there is a pressure contribution both from the CO_2 in the chamber and the saturation pressure of H_2O, which is at most ~200 Pa at 260 K. Assuming the pressure difference across the sample equals the saturation vapor pressure, p_0 = 800 Pa. This overly pessimistic pressure difference leads to a barodiffusion contribution of less than 15% of the size of the concentration diffusion.

[54] None of the coefficients $\mathcal{D}_{12}$, $\mathcal{D}_T$, and $\mathcal{D}_p$ depend on gravity, nor does the advective contribution. The potential energy $m_1 g\Delta z$ required to move molecules through the diffusive barrier, or through meters of regolith, is negligible compared with their kinetic energy $(3/2)kT$.

[55] Adsorption can significantly effect the transport of water in a non-steady-state environment by attenuating local vapor density gradients and acting as either a source or a sink for water vapor. We shall discuss these effects in section 6 and show that they are not important on the timescales which we consider.

3. Experimental Setup and Measurements

[56] Experiments were conducted at the Ice Lab facility in the Geological and Planetary Sciences department of Caltech. This facility is equipped for sample preparation and features two walk-in freezers with nominal temperatures of approximately −10°C and −20°C, and a cold-box capable of temperatures below −80°C. Custom built vacuum chambers of plastic or stainless-steel construction were used to achieve Mars-like pressures and controlled humidity environments within the freezers.

3.1. Sample Materials

[57] The Martian regolith is a complex substance. Early lander-based measurements of elemental composition show close similarity among widely spaced sites [*Arvidson et al.*, 1989]. Despite discoveries by both Viking and the MER mission that reveal significant chemical and physical differences among the nonrocky components of the surface [*Moore et al.*, 1979], they are very similar in absolute terms over planetary-scale distances. Various investigators have used the JSC Mars−1 palagonite ash from Mauna Kea to simulate Mars regolith in a variety of experiments [*Gilmore et al.*, 2004; *Cooper and Mustard*, 2002; *Gross et al.*, 2001]. Martian soils no doubt come in a variety of grain size distributions, grain shapes, porosities, compositions, and degrees of compaction and cementation. With respect to the demonstrably heterogeneous Martian regolith, the Mars−1 soil is not assumed to match a particular locality on Mars, but rather is a complex, natural soil material which may represent a general class of Mars regolith. A thorough description of JSC Mars−1 are given by *Allen et al.* [1997, 1998].

[58] JSC Mars−1 contains a variety of minerals which exhibit different patterns of fracture, cleavage, and surficial chemical structure making this a very complex regolith simulant. The JSC Mars−1 simulant can be easily characterized, but the parameter space to be explored is vast. Working with fine-grained granular media presents many challenges, particularly with regards to repeatability. To eliminate some of the complexities involved in studying a chemically and physically heterogeneous disaggregated powder, some simpler and more easily handled proxies for porous regolith materials are used initially. (1) The 40−70 μm beads are our standard sample, obtained from AGSCO Corporation, with narrow particle size distribution and composed of soda lime glass (specific gravity: 2.50). (2) "Coarse" frits denote consolidated media, porous filter disks from ChemGlass Inc., with pore size between 50 and 80 μm and sintered borosilicate glass (specific gravity: 2.53). (3) The 1−3 μm dust comprises smaller particles, obtained from Powder Technology Inc., with narrow particle size range of equant yet angular particles and natural silicate mineral (specific gravity: 2.65). (4) JSC Mars−1 denotes weathered palagonitic cinder-cone ash, obtained through JSC Curator, with wide particle size distribution from 1 mm to <1 μm and complex mineralogy (average specific gravity: 1.91).

[59] Wind-blown sand particles on Mars were proxied by the glass beads, whose size range is similar to that observed in Mars wind-tunnel experiments and at MER landing sites (see section 5.1.1). The Arizona Test Dust approximates size characteristics of dust on Mars. The porous frits were chosen to illustrate experimental repeatability given a medium with an unchanging geometry. JSC Mars−1 was selected because it has been frequently used in other investigations of Mars analogue materials.

[60] See Figure 2 for optical micrographs of these simulants at the same scale. Prior to use, all samples are dried in an oven at 110°C and then stored in air tight containers.

[61] The source of water vapor in these diffusion experiments is a block of ice made from purified water. The ice is frozen in the presence of both a heat source to retard surface freezing and a bubbler to provide mechanical agitation. This procedure allows most gases exsolved upon freezing to escape through the top surface, resulting in a cylinder of largely bubble-free ice.

[62] Ice samples are cut from the cylinder in 1 cm thick slices and frozen with a small amount of additional water into plastic caddies ~7 cm in diameter and of various heights (2, 3, 6, and 11 cm), permitting sample thicknesses over the ice of 1, 2, 5, and 10 cm, respectively. A T-type thermocouple wire passes through the caddy wall 1 cm from the bottom and extends to the center of the cylinder. This wire is positioned on the surface of the ice disk and frozen into place, allowing the tip to remain in contact with the ice during the first 2−4 mm of retreat. See Figure 3a for a close-up of thermocouple positioning.

3.2. Chamber Setup

[63] A custom built stainless-steel vacuum chamber from LACO Technologies was used to perform the experiments at −10°C. In basic design the chamber is a vertical cylinder with a removable lid, silicone O-ring seals, and multiple electrical and fluid feedthroughs. The volume of the chamber is 2.3×10^{-2} m^3.

[64] During an experiment, an Alcatel rotary vacuum pump continuously pumps on the chamber at an effective pumping speed of 0.34 m^3 per hour. The pressure is

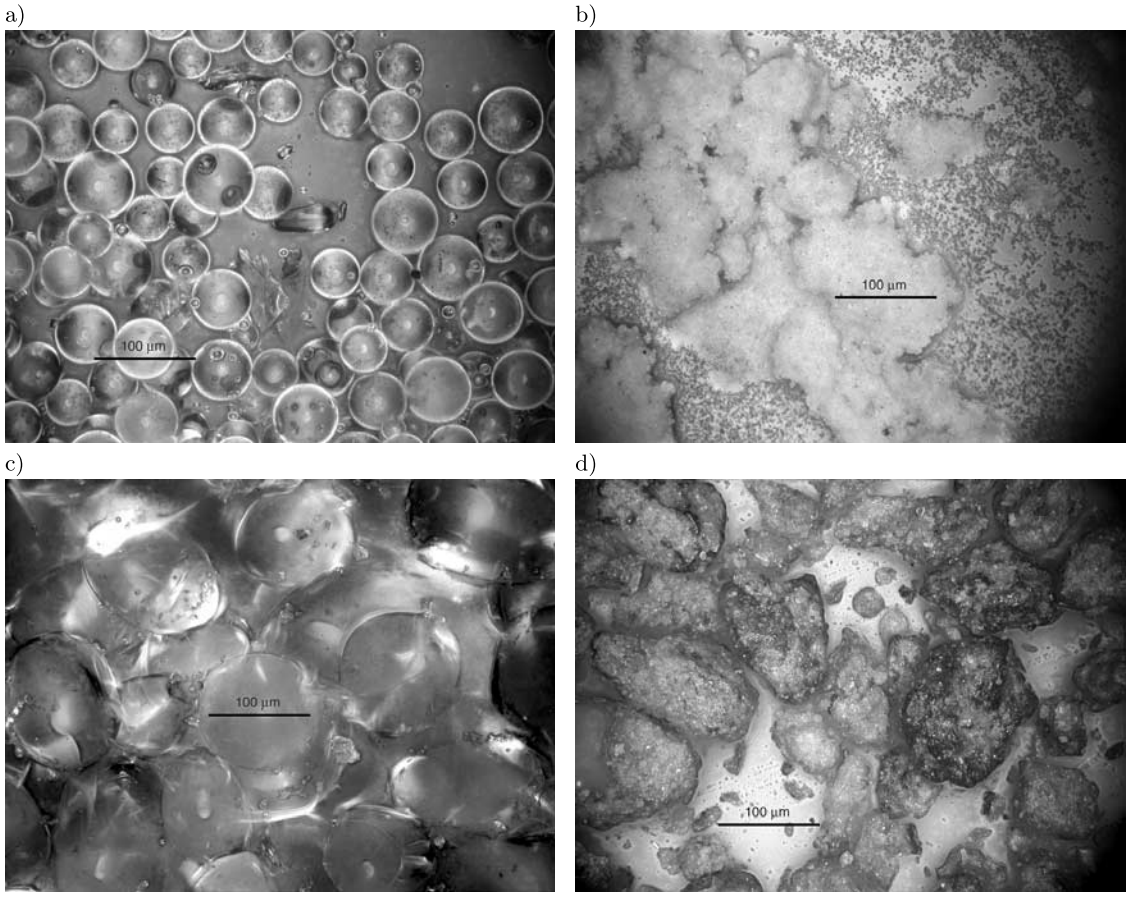

Figure 2. Optical micrographs of regolith simulants: (a) 40–70 μm beads, (b) 1–3 μm Arizona Test Dust (note the presence of aggregates), (c) "Coarse" fritted disks, pore size 50–80 μm, and (d) JSC Mars–1.

monitored with a Barratron capacitance manometer with a full-scale range of 10 torr. Evacuation is compensated by input of dry CO_2 regulated with an MKS PDR 2000 gauge controller connected to a normally open solenoid valve. The total pressure is maintained at ~600 Pa. The continuous replacement of chamber gas results in a very dry atmosphere above the samples (see Figure 3b).

[65] Decompression of the dry CO_2 into the cold chamber produces a stable chamber air temperature of approximately −12°C. The walk-in freezer is on a 12-hour defrost cycle which results in twice-daily temperature spikes of approximately 0.5°C. These perturbations to the environment decay in about 60 min. Fiberglass and Styrofoam insulation around the chamber minimizes these fluctuations.

[66] Water content in the chamber atmosphere is monitored using capacitive relative humidity (RH) chips from Honeywell (HIH-3602-C). These integrated-circuit sensors contain both an RH proportional voltage output and a 1000 ohm

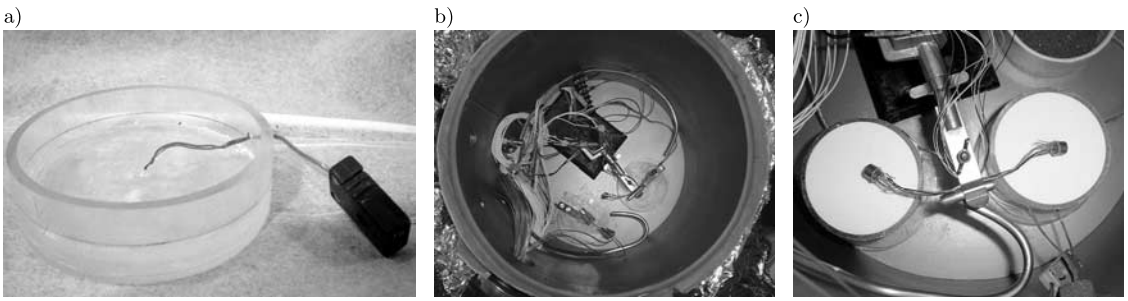

Figure 3. (a) Closeup of thermocouple positioning in a caddy designed to accommodate 1 cm of ice and a 1 cm sample. The caddies are ~7 cm in diameter. (b) Down-looking view into the stainless steel chamber (30 cm diameter) showing two load cells, gas and electrical feedthroughs, and RH/RTD chips attached to a ring-stand for positioning. (c) A closeup of two glass bead samples in place with RH/RTD chips positioned 1 cm above sample surfaces.

platinum resistance temperature device (RTD) which is measured in a 3-wire half-bridge configuration. The RH chips are reported to be accurate down to temperatures of −40°C and 0% relative humidity. The combined RH and temperature measurements allow the partial pressure of water at the sensors to be calculated. The sensors are positioned at the center of the sample top within 1 cm of the surface (see Figure 3c).

[67] Sample mass is continuously monitored with Omega Engineering LCEB-5 strain gauge load cells (maximum capacity 5 lbs) in a wheatstone bridge configuration with an excitation of 5 V and an output of 2.0 mV/V. This instrument has a noise level of 0.2% of reading and a 0.03% full-scale linearity. Mass-loss rates are calculated by monitoring the sample mass and drawing a linear regression through the values obtained over many hours.

[68] The data from an experiment are recorded with a Campbell Scientific CR1000 data logger and saved to computer via the LoggerNet software package. Currently, we are able to perform two simultaneous experiments in the vacuum chamber with dual load cells, thermocouples, and RH/RTD chips. A second setup of slightly different construction and capable of only one experiment at a time exists in the −20°C freezer. This chamber was built in-house out of 3/8-inch lucite plastic and seals with silicone O-rings. This 7.3×10^{-3} m^3 chamber is evacuated by a separate Welch rotary pump and has its own CO_2 inputs, electrical feeds, load cell, and sensors. Data from this chamber are recorded on a Campbell Scientific CR10X data logger.

3.3. Sample Preparation and Experimental Method

[69] Unconsolidated samples are prepared in the following manner. Centimeter thick bubble-free ice disks are frozen in place at the bottom of the sample cylinders as described at the end of section 3.1. The mass of the ice-containing caddy is measured with a precision balance; the mass of the caddy plus thermocouple is known. The total mass of ice and thereby its volume and thickness in the caddy can be determined. A predried sample is emplaced over the ice, packed as desired, and planed off to form a flat surface. The total mass of the entire sample assembly is measured, giving the total mass of simulant. The sample assembly is connected to the thermocouple feedthrough and placed on the load cell within the chamber. Finally, the RH/RTD sensor is positioned above the sample. The chamber is then sealed and pumped down to 600 Pa at a rate of ∼100 Pa per second. This slow pump-down prevents disturbance of the sample as any interstitial gases escape.

[70] All steps described above are performed in the walk-in freezer. The relative humidity of the freezer interior is quite high, usually around 80%, but the absolute humidity is low. Exposure of the samples to freezer air for the brief period between the storage vessel and the start of an experiment does not allow significant amounts of water to adsorb or freeze onto the simulant (as confirmed by water content measurements). Surface-melting, capillarity, and their effects on the initially dry simulant are thus minimized.

[71] Once the samples are in place and the chamber has reached Mars pressures, the experiment is left to run for at least 12 hours. Transients due to adsorption of water in the sample or temperature disequilibrium are gone after approximately two hours. The faster the mass-loss rate from the sample, the less time is needed to obtain a sufficient number of points to ensure linearity and draw a regression line. For samples with a high impedance to gas flow, up to three days may be needed to achieve a high degree of confidence in the measurements.

[72] Following the completion of an experimental run, the chamber is slowly (to prevent air currents from disturbing the sample) purged to room pressure. The sample material is dumped into a metal or glass vessel which is immediately weighed, then placed into an oven at 110°C. After 24 to 48 hours the sample is completely dry with respect to non-structural water (which is also zero in the case of glass beads or frits) and is weighed again. The sample is now dry and may be recycled for future experiments.

3.4. Measured Quantities

[73] All data for calculating diffusion coefficients reported herein is taken from the stable interval following initial transients. Additional small perturbations in temperature are due to defrost cycling of the compressor in the freezer every 12 hours. These have no apparent effect on the mass loss curve and have a very small contribution to the average temperature value calculated for a 12+ hour experiment.

[74] The mass loss rate is derived from a least-squares fit to the post-transient weight data versus time (see Figure 4). The temperature of the load cell fluctuates less than 1°C; there is no sensible temperature effect on the values reported. Residuals to the linear fit of mass loss are less than 1% in all experiments. Given the area of the sample surface (39.8 cm^2) and the density of ice, retreat rates in mm/hr and total H_2O flux are calculated.

[75] Ice surface temperature is monitored as described above. We assume that the vapor at the surface of the ice is saturated with respect to water vapor. This temperature thus gives the saturation vapor pressure of H_2O via the ITS-90 formulation for vapor pressure [*Hardy*, 1998]. Figure 4 shows ice surface temperature as a function of time for one experiment.

[76] The RH/RTD sensors simultaneously report water activity a_w and ambient temperature at the sensor. Figure 3c shows examples of placement and Figure 4 shows the data as reported. Capacitive sensors such as the HIH-3602 are responsive to water activity rather than to relative humidity [*Anderson*, 1995; *Koop*, 2002]. The difference is that water activity is the ratio of vapor content of the atmosphere p_1 to the saturation vapor pressure over liquid water rather than over ice,

$$a_w = p_1 / p_{sv}^{liq}. \tag{24}$$

Thus the true relative humidity is given by

$$RH = p_1 / p_{sv}^{ice} = a_w p_{sv}^{liq} / p_{sv}^{ice}. \tag{25}$$

[77] The equation for p_{sv}^{liq} is determined from data on supercooled water taken from *Hare and Sorensen* [1987]. The ITS-90 formulation is used for p_{sv}^{ice} to determine *RH*, and then used again to convert the relative humidity

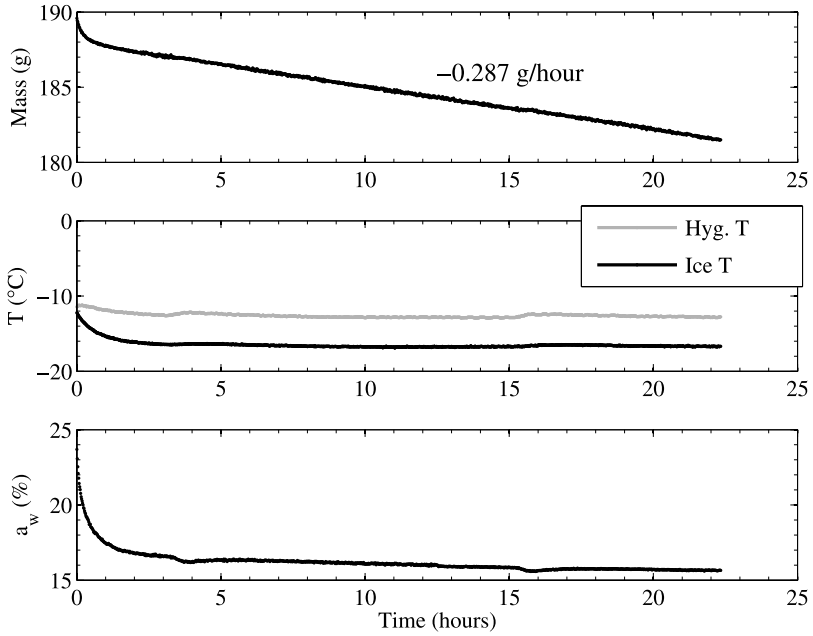

Figure 4. Data for a single sample: 17 February 2006. Conditions: 40 μm glass beads, 2 cm thick, T $\approx$ -10°C. The mass loss rate displayed in the top axis is determined from a linear regression to post-transient data.

calculated above the sample into a partial pressure of water via the ideal gas law.

4. Data Analysis Methods

[78] This section details the procedure for reducing data from each experiment into diffusion coefficients. Figure 5 is a schematic drawing of the experimental setup with different levels in the sample column labeled A through D. Although our unconsolidated samples always rest directly on the ice, we generalize the schematic to allow for a gap between positions A and B. A formalism to determine a correction term to account for gas gaps, sublimation effects, and true sample thickness is described below. An analysis method for the diffusion regime and pressure dependence of the diffusion coefficient is also presented.

4.1. Determining the Diffusion Coefficient

[79] Equation (6) is valid in the limit where c, and therefore advection, is small. This is used to extract the diffusion coefficient from measurements above (position "D" in Figure 5) and below (position "A" in Figure 5) the soil sample,

$$J_1 = D' \frac{\rho_{1A} - \rho_{1D}}{\Delta z}, \tag{26}$$

where D' is the "raw" diffusion coefficient. The vapor density above the sample ρ_{1D} is determined from measurements of temperature and humidity in the air which gives a partial pressure of water vapor p_{1D}, and thereby $\rho_{1D} = p_{1D}M_1/RT_D$. Vapor density at the ice surface is calculated from the saturation vapor pressure determined from the measured ice temperature, $\rho_{1A} = p_{sv}^{ice} M_1/R\ T_A$.

4.2. Correcting the Diffusion Coefficient

[80] When vapor is not diffusing through a porous medium it may still encounter resistance. To undergo gas-phase transport, H_2O molecules must first sublime from the ice surface into vapor. This vapor must then diffuse through a boundary layer and any intervening gas between the ice and sample surfaces. After passing through the sample, this vapor must pass from the sample surface to the hygrometer. These gas layers may not be well mixed, resulting in an underestimated diffusion coefficient. Additionally, the measured thickness of the samples is only from B to C, not from A to D. The diffusion coefficient defined in equation (26) is therefore referred to as the raw diffusion coefficient. A

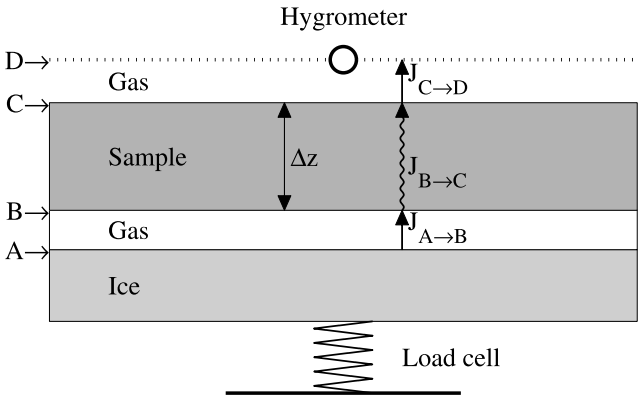

Figure 5. Generalized schematic of experimental setup showing gas gaps separating both the ice surface and hygrometer (RTD/RH chip) from the sample. By continuity, the vapor flux through the sample is the same as that through the gaps.

correction to the raw diffusion coefficient for the effects of sample thickness, sublimation effects, and gas gaps may be performed given sufficient data.

[81] By conservation of mass, the flux of vapor is the same through all three barriers $J_{A \rightarrow B} = J_{B \rightarrow C} = J_{C \rightarrow D} \equiv J_1$ (see Figure 5). Assuming that the fluxes between A and B and between C and D are still proportional to the density gradient, $J_1 = J_{A \rightarrow B}$ can be used to determine ρ_{1B} and $J_1 = J_{C \rightarrow D}$ can be used to determine ρ_{1C}, while ρ_{1A} and ρ_{1D} are measured. Substituting these into an expression analogous to equation (26) and simplifying, the resulting corrected expression for the diffusion coefficient in the sample is

$$J_1 = D\frac{\rho_{1B} - \rho_{1C}}{\Delta z} = D\frac{\rho_{1A} - \rho_{1D}}{\Delta z + z_{corr}}. \quad (27)$$

The quantity z_{corr} has units of length and accounts for effects other than diffusion through the porous medium including gas-gas diffusion in gaps above and below the sample and any sublimation limitation.

[82] The correction term z_{corr} can be determined if several measurements of identical samples with different thicknesses are available. By recasting the corrected expression, equation (27), as linear in terms of sample thickness Δz

$$\frac{\Delta\rho_1}{J_1} = -\frac{\Delta z}{D} - \frac{z_{corr}}{D}, \quad (28)$$

a linear fit can be performed and the constants z_{corr}/D and $1/D$ determined by the intercept and slope, respectively. The same correction term should apply to all experiments with the same temperature, pressure, and sample type. We can now use z_{corr} with the right hand side of equation (27) to solve for corrected individual values of D. Since the total vapor density gradient is smaller for thinner samples, the relative contribution of the gas gap is larger and the necessary correction $1/(\Delta z + z_{corr})$ will likewise be larger. The thickness for which the correction is negligible compared to systematic scatter is between 2 and 5 cm for the glass beads.

4.3. Diffusion Regime

[83] At intermediate pressures when both collisions with other molecules and with the pore walls are important, the diffusion is said to be in transition between the Fickian and Knudsen regimes. The Bosanquet interpolation derived in equation (16) says that the effective diffusion coefficient D is made up of contributions from both a pressure-dependent Fickian diffusion term and a Knudsen term

$$\frac{1}{D(p_0)} = \frac{p_0}{p_{ref} D_F(p_{ref})} + \frac{1}{D_K}, \quad (29)$$

where we have explicitly written the pressure dependence of the Fickian term in terms of the value of D_F at a particular reference pressure p_{ref}. Substituting equation (29) into (26) produces the complete expression for flux in terms of pressure and two diffusion coefficients,

$$J_1 = \frac{1}{\frac{p_0}{p_{ref} D_F(p_{ref})} + \frac{1}{D_K}} \frac{\rho_{1A} - \rho_{1D}}{\Delta z}. \quad (30)$$

If data is taken at a number of different pressures, the parameters $D_F(p_{ref})$ and D_K may be fit to the flux data using a nonlinear least squares algorithm.

5. Results

[84] We present here the first diffusion coefficients measured for unconsolidated porous media under simultaneous conditions of low pressure and temperature appropriate to Mars surface and shallow-subsurface studies. Four simulant materials are considered. The largest data set available is for the 40–70 μm beads. Limited investigations were also performed on three other simulant materials: porous glass filter disks (frits), JSC Mars–1, and 1–3 μm dust.

5.1. The 40–70 μm Glass Beads at −10°C

[85] Data for this simulant are shown in Table 2.

5.1.1. Sample Characteristics

[86] As seen in the optical micrograph image in Figure 2a, the bead particles are all nearly perfect spheres in the size range 40–70 μm. Within a factor of two in friction threshold velocity, these are similar to the 100 μm size of the most easily lofted particles under Martian conditions [*Greeley et al.*, 1980]. Terrestrial analogs and wind-tunnel experiments suggest that suspended dust is usually not incorporated into sand dunes, and Spirit Microscopic Imager pictures indicate that sand sheets in Gusev crater are largely composed of fine to medium sand-sized particles. At least 70% of the beads fall within the size range given, with no more than 10% being larger, no more than 20% being smaller, and no more than 3% being broken or angular in shape.

[87] Pore sizes may be estimated from particle size. Between three coplanar spherical particles of the same radius, the theoretical minimum pore size is $r_{min} = r_{particles}(3\sqrt{3}/4 - 1)$. The largest dimension between kissing points in a cubic packing of spheres is the diameter d. Between such wide openings the pore space constricts to only $d(\sqrt{2} - 1)$ when passing between one cubic unit cell to the next. Thus for a mixture of beads with 40–70 μm close-packed particles, the minimum pore size is 11.96 μm and the maximum is 70 μm. With a mean free path of $\sim$12 μm under experimental conditions, this gives a ratio of r/λ_1 from 1.0 to greater than 2.4. Close-packing may not obtain throughout the sample and larger irregular pores are likely. Thus we expect that diffusion will be dominated by Fickian processes of molecule-molecule collisions, but that Knudsen interactions between molecules and the pore walls will also play a role.

5.1.2. Diffusion Coefficient

[88] Experiments were run for several thicknesses and a regression was calculated to determine the correction term as described in section 4.2. The correction term is $z_{corr} = 0.58 \pm 0.07$ cm. The raw and corrected diffusion coefficients are plotted in Figure 6. The uncorrected diffusion coefficient is moderately correlated with sample thickness (R = 0.57). Applying the correction term z_{corr} to the calculation of D nearly eliminates the correlation (R = −0.02).

[89] The weighted mean of the corrected diffusion coefficients is 4.49 cm^2 s^{-1}, with a weighted standard deviation of 0.69 cm^2 s^{-1}. Raw values from 5 and 10 cm samples are indistinguishable from this range. If we use the dependence

Table 2. Experimental Conditions, Data, and Corrected Diffusion Coefficients for 40–70 μm Glass Beads at ~600 Pa

Conditions	Date	Δz, cm	p_0, Pa	T_{ice}, K	T_{air}, K	RH, %	J_1, mg m^{-2} s^{-1}	$\bar{c}$	$\Delta\rho_1$, g m^{-3}	D, cm^2 s^{-1}	$D/\mathcal{D}_{12}$
−10°C CO_2	28 Nov	1.03	612	256.9	260.8	20.56	27.25	0.072	0.88	5.02 ± 0.66	0.20 ± 0.03
	5 Dec	1.05	611	256.7	261.2	11.13	20.44	0.065	1.02	3.27 ± 0.41	0.13 ± 0.02
	8 Dec	0.99	634	256.6	260.8	15.57	19.71	0.064	0.94	3.31 ± 0.41	0.13 ± 0.02
	15 Dec	1.06	584	256.3	260.2	13.06	26.00	0.066	0.96	4.47 ± 0.53	0.17 ± 0.03
	15 Dec	0.93	584	256.7	260.3	12.35	29.83	0.068	1.01	4.47 ± 0.54	0.17 ± 0.03
	6 Feb	1.02	630	254.5	260.1	19.65	22.51	0.056	0.68	5.31 ± 0.73	0.22 ± 0.03
	16 Dec	2.10	596	257.4	260.8	12.92	20.60	0.072	1.07	5.15 ± 0.52	0.20 ± 0.02
	16 Dec	1.92	596	256.7	260.8	7.38	22.63	0.063	1.09	5.21 ± 0.51	0.20 ± 0.02
	17 Dec	2.10	598	257.5	260.9	7.93	19.19	0.069	1.17	4.41 ± 0.42	0.17 ± 0.02
	17 Dec	1.92	598	257.1	260.9	13.35	22.12	0.070	1.02	5.41 ± 0.56	0.21 ± 0.03
	7 Feb	1.87	598	256.5	260.7	15.29	17.77	0.068	0.94	4.64 ± 0.50	0.18 ± 0.02
	7 Feb	1.85	598	256.2	260.5	16.57	20.05	0.067	0.88	5.54 ± 0.62	0.21 ± 0.03
	14 Feb	2.08	594	257.1	261.1	14.98	17.46	0.072	0.99	4.69 ± 0.50	0.18 ± 0.02
	14 Feb	2.15	594	256.7	261.0	17.74	19.62	0.072	0.90	5.95 ± 0.66	0.23 ± 0.03
	17 Feb	1.74	592	256.6	260.5	18.05	20.14	0.071	0.90	5.17 ± 0.59	0.20 ± 0.03
	17 Feb	1.71	592	256.1	260.3	19.48	20.86	0.069	0.83	5.75 ± 0.68	0.22 ± 0.03
	16 Sep	4.76	571	259.1	262.0	10.63	12.71	0.088	1.30	5.24 ± 0.46[a]	0.19 ± 0.04
	22 Sep	4.95	586	259.2	262.1	13.83	11.11	0.090	1.25	4.93 ± 0.45[a]	0.18 ± 0.03
	18 Dec	4.94	595	259.3	261.5	5.18	12.71	0.082	1.44	4.87 ± 0.40	0.18 ± 0.02
	18 Dec	4.97	595	259.5	261.5	4.55	9.57	0.082	1.47	3.61 ± 0.29	0.14 ± 0.02
	9 Jan	5.04	603	259.6	261.5	4.72	9.75	0.082	1.49	3.68 ± 0.30	0.14 ± 0.02
	9 Jan	5.14	603	259.8	261.4	5.52	10.21	0.084	1.50	3.90 ± 0.32	0.15 ± 0.02
	8 Feb	4.95	594	259.0	261.4	7.34	12.30	0.081	1.36	5.01 ± 0.42	0.19 ± 0.02
	8 Feb	4.91	594	258.9	261.2	5.48	10.36	0.078	1.38	4.13 ± 0.34	0.16 ± 0.02
	9 Dec	10.13	616	260.5	261.6	6.07	7.37	0.089	1.58	4.98 ± 0.39	0.20 ± 0.03
	9 Dec	10.11	616	260.3	262.7	3.84	6.09	0.086	1.59	4.10 ± 0.32	0.16 ± 0.02
	20 Dec	9.98	575	260.3	261.6	3.17	7.10	0.093	1.62	4.64 ± 0.35	0.17 ± 0.02
	20 Dec	9.97	575	260.3	261.5	3.51	6.38	0.094	1.61	4.17 ± 0.32	0.15 ± 0.02
	10 Feb	9.90	580	260.0	261.6	6.67	5.98	0.092	1.50	4.17 ± 0.33	0.15 ± 0.02
	10 Feb	9.69	580	259.9	261.5	7.87	8.95	0.092	1.48	6.22 ± 0.50	0.23 ± 0.03
	18 Feb	9.84	583	260.0	261.5	8.20	7.07	0.092	1.48	4.99 ± 0.41	0.19 ± 0.02
	13 Apr	9.87	589	259.8	261.5	8.43	6.03	0.089	1.44	4.37 ± 0.36	0.16 ± 0.02
	13 Apr	9.79	588	259.8	261.3	7.95	7.74	0.087	1.45	5.54 ± 0.45	0.21 ± 0.02
−20°C CO_2[b]	3 Apr	2.08	592	248.4	248.4	22.40	8.19	0.029	0.44	3.87 ± 0.59	0.21 ± 0.03
	22 Mar	5.02	572	249.5	251.1	10.45	3.83	0.031	0.55	3.49 ± 0.16	0.15 ± 0.02
	27 Mar	4.96	585	249.7	251.3	11.10	5.69	0.031	0.56	5.04 ± 0.30	0.23 ± 0.02
	29 Mar	4.96	602	249.5	251.2	13.87	5.03	0.031	0.53	5.73 ± 0.31	0.22 ± 0.02
	31 Mar	4.96	610	249.8	251.3	14.75	5.11	0.031	0.53	4.75 ± 0.27	0.22 ± 0.02
−10°C N_2	4 Jan	0.94	625	256.1	259.8	14.57	31.55	0.061	0.92	5.57 ± 0.88	0.22 ± 0.03
	4 Jan	0.92	625	256.6	259.9	11.21	33.33	0.062	1.02	5.24 ± 0.76	0.21 ± 0.03
	6 Jan	10.01	637	260.1	261.5	3.73	8.59	0.082	1.57	5.84 ± 0.18	0.23 ± 0.02
	6 Jan	9.85	637	260.0	261.5	5.38	7.13	0.083	1.54	4.89 ± 0.14	0.19 ± 0.02

[a]Experiments on 16 and 22 September were carried out in a plastic vacuum chamber built in-house.
[b]The z_{corr} was not calculated for −20°C experiments; uncorrected diffusion coefficients, D', reported.

of diffusion coefficient on temperature of $T^{3/2}$ as appropriate for Fickian diffusion and choose a typical Mars temperature of 200 K, we obtain $D(200\ \text{K}) = 3.06 \pm 0.47\ \text{cm}^2\ \text{s}^{-1}$.

[90] For the diffusion coefficient of a free gas scaled to the appropriate temperatures and pressures, we use the formula given by *Wallace and Sagan* [1979], with a 6% error to account for differences between this and other calculations of $\mathcal{D}_{12}$. For glass beads at 600 Pa and 260 K, the calculated $\mathcal{D}_{12}$ is $26.4 \pm 0.7\ \text{cm}^2\ \text{s}^{-1}$.

[91] Experiments were conducted on columns of loose glass beads with thicknesses of 1 and 10 cm under an N_2 atmosphere instead of CO_2. A correction term of $z_{corr} = 0.70 \pm 0.14$ cm was calculated and applied to these samples. The weighted mean of corrected diffusion coefficients determined under a CO_2 atmosphere is $4.62\ \text{cm}^2\ \text{s}^{-1}$ for 10 cm columns. The same value for N_2 is $5.25\ \text{cm}^2\ \text{s}^{-1}$. According to equation (9) the diffusion coefficient in N_2 should be larger than in CO_2 by a factor of approximately 1.4, that being the ratio of their mutual gas diffusion coefficients for H_2O in the two gases as calculated using the expression of Holman in section 2.2. The difference observed is a factor of 1.14. Though somewhat smaller than the expected difference, the change in diffusion coefficients is of the right magnitude and direction. The agreement between obstruction factors in glass beads under different host gases but similar conditions of temperature and pressure (see Table 2) validates our data analysis method.

5.1.3. Errors and Scatter

[92] Formal errors in the diffusion coefficient are calculated by taking partial derivatives of equation (27) with respect to five measurable quantities: z, z_{corr}, J_1, ρ_{1A}, and ρ_{1D}. Each contributing partial is then sum-squared to give the total error in D. Flux error derives from mass loss errors, which are the standard deviations of all post-transient data points with

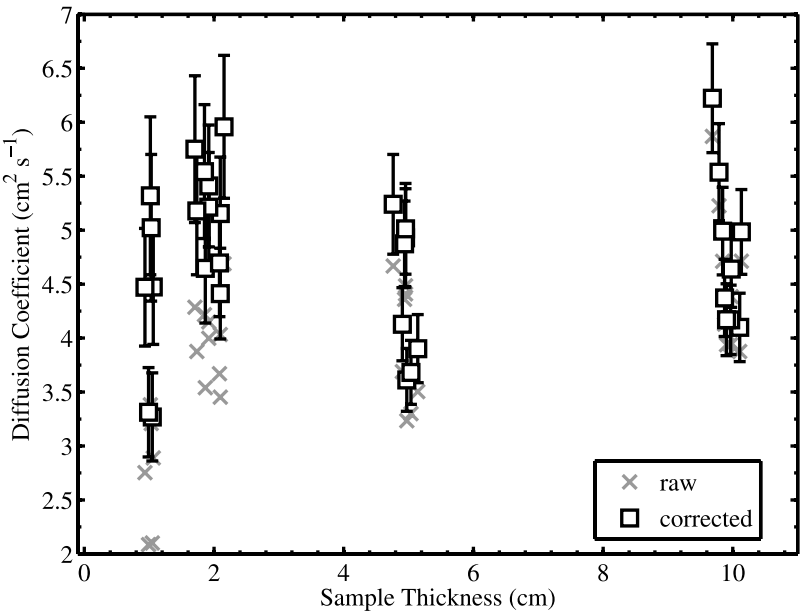

Figure 6. Measured and corrected diffusion coefficients for 40–70 μm glass beads at −10°C and 600 Pa. The influence of boundary layer diffusion decreases as the sample thickness (i.e., resistance) increases. The correlations between D' (raw data) and thickness are 0.57, but only −0.02 between D (corrected data) and thickness.

respect to the linear regression. Sample thickness is constant throughout an experiment and its deviation is estimated as a ±1 mm measurement error in all cases.

[93] Humidities, total pressures, and temperatures are ideally constant throughout the duration of an experiment, but do in fact exhibit some degree of variation. Errors in ρ_{1D} and ρ_{1A} are taken from contributing errors in T_{ice}, T_{air}, RH, and p_0. Experiments with multiple thermocouples show variations in T_{ice} on the order of 0.4°C from the sample edge to its center. The error, dT_{ice}, is the greater of the standard deviation of the measurement of T_{ice} and 0.4°C. The error is no greater than 0.46°C for any experiment. The error in saturation vapor pressure at the ice surface is the difference between the saturation vapor pressures calculated at $T_{ice} + dT_{ice}$ and $T_{ice} - dT_{ice}$. This makes the error in p_{H_2O} at the ice surface a conservative overestimate. Errors in the quantities T_{air}, RH, and p_0 are taken as the standard deviation about their mean.

[94] Less than 2% of the error in the value of D for each experiment comes from z_{corr}, J_1, and ρ_{1D}. The dominant errors are those in z and ρ_{1A}, which range from 1 to 8% of the value of D. For all experiments the combined error is less than the value of D by a factor of ten or more.

[95] The greatest uncertainty in these experiments comes from systematic variation between experimental runs. Variations in input parameters to the diffusion coefficient such as thickness, relative humidity, temperature, pressure, and flux should be accounted for by the calculations since the expressions for D explicitly or implicitly include these parameters. Scatter may therefore arise for two reasons.

[96] First, effects arising from advection, gas composition, and barrodiffusion may not be as minor as we have calculated and could contribute to each experimental run a flux unaccounted for in our present methodology. As stated above, we believe the maximum contribution of any of these individual effects to be on the order of 10%.

[97] Second, there may be errors arising from changes in the experimental setup itself. The largest variation in measured quantities among samples of a given thickness is in relative humidity, which may vary by between 25–48% among individual experiments. Repositioning or substituting sample vessels may affect the airflow of dry and moist gases in the overturning chamber atmosphere. Water vapor densities at the surface of the sample may not be uniform in the horizontal or vertical directions and the relative humidity measured by the hygrometer may not reflect the environment across the majority of the sample surface.

[98] Nevertheless, enough experiments have been run to allow us to give confident bounds on our measured diffusion coefficients, though in some cases apparent outliers still have a discernible effect on the averages.

5.1.4. Variable Pressure Experiments

[99] Experiments were performed at 300, 600, 1200, 3000, and 6000 Pa using a 5 cm column of 40–70 μm beads; the data are presented in Table 3. Since we do not have measurements at many thicknesses for each pressure, we cannot apply a correction term to the variable pressure data; we do not assume that the correction term for glass beads is the same at all pressures. We do assume, however, that 5 cm is enough thickness to make the correction contribution small at all pressures measured. Pressures less than ~250 Pa were not used; at these lower pressures the vapor pressure of the ice becomes a significant fraction of the total chamber pressure and the experiment is no longer in a predominantly diffusive mode. We compare the fit calculated using the method in section 4.3 to calculated (uncorrected) diffusion coefficients in Figure 7.

[100] The fit parameters determined are $D_F(p_0) = 6.5$ (600 Pa/p_0) cm^2 s^{-1} and $D_K = 9.8$ cm^2 s^{-1} and are shown as solid lines in Figure 7. The transition pressure, where $D_F(p_0) = D_K$ is found to be at 398 Pa. The transition pressure corresponds to a mean free path of 18 μm, which is near the

Table 3. Experimental Conditions and Diffusion Coefficients for 5 cm Samples of 40–70 μm Beads at −10°C and Various Pressures[a]

Date	Δz, cm	p_0, Pa	T_{ice}, K	T_{air}, K	RH, %	J_1, mg m^{-2} s^{-1}	$\bar{c}$	$\Delta\rho_1$, g m^{-3}	D', cm^2 s^{-1}	$D'/\mathcal{D}_{12}$
21 Mar	4.79	294	257.6	260.8	11.64	13.14	0.178	1.22	5.61 ± 0.50	0.11 ± 0.01
21 Feb	4.95	1173	260.2	261.8	7.41	7.24	0.041	1.52	2.37 ± 0.19	0.18 ± 0.02
21 Feb	4.92	1173	260.1	261.7	7.44	7.88	0.041	1.51	2.58 ± 0.21	0.19 ± 0.02
29 Mar	4.86	2917	260.8	261.5	13.58	3.46	0.018	1.49	1.13 ± 0.10	0.21 ± 0.02
14 Mar	4.98	5875	261.3	261.6	5.99	1.25	0.008	1.71	0.37 ± 0.03	0.14 ± 0.01
14 Mar	4.94	5875	261.2	261.4	4.87	3.88	0.008	1.73	1.11 ± 0.09	0.42 ± 0.04
16 Mar	4.98	5880	261.0	261.5	5.05	1.41	0.008	1.68	0.42 ± 0.03	0.16 ± 0.02
16 Mar	4.94	5880	261.1	261.4	6.71	2.89	0.008	1.68	0.85 ± 0.07	0.33 ± 0.03
27 Mar	4.96	5899	261.3	261.7	12.50	1.80	0.009	1.59	0.56 ± 0.05	0.21 ± 0.02
27 Mar	4.82	5899	261.3	261.6	13.08	1.78	0.009	1.58	0.54 ± 0.05	0.20 ± 0.02

[a]The 600 Pa data are reported in Table 2. A correction term was not determined for pressures other than 600 Pa; the values reported as D' are therefore raw values. These data are plotted in Figure 7 along with nonlinear fit parameters for $D_F(p_0)$ and D_K.

smaller end of the estimated pore size distribution. Mars surface pressures fall between the extremes measured, and are quite close to the transition pressure, placing materials of similar porosity and tortuosity to our 40–70 μm simulant in the transition regime.

[101] At the beginning of this subsection, experiments performed at 600 Pa, with a mean free path of ~12 μm, were shown to be within the diffusion transition regime. If the pressure is increased to 1200 Pa, the mean free path is only 5.9 μm, placing the largest pores within the Fickian regime; an increase to 5700 Pa should guarantee Fickian flow. Conversely, diffusive transport at 50 Pa would bring the smallest pores into pure Knudsen flow, but the bulk of the sample would still be in transition.

5.1.5. Porosity and Tortuosity

[102] The measured sample masses and their volumes are ratioed to determine a bulk density. Dividing by the true density of the component materials (2.5 g cm^{-3} in the case of glass beads) results in a geometric porosity. The porosity calculated may be an overestimate if some pore spaces are unavailable for gas transport. The range of porosities calculated for the 40–70 μm beads is from 41% to 49%, with a mean value of 44 ± 2%.

[103] The six high-pressure experiments with $\bar{P}$ = 5890 Pa should fall within the Fickian diffusion regime. The theoretically calculated gas-gas diffusion at this pressure is 2.67 ± 0.2 cm^2 s^{-1}. The diffusion coefficient determined from the fit in section 5.1.4 obtains $D_F(5890)$ = 0.66 cm^2 s^{-1}. This gives an obstruction factor of 0.25 ± 0.02. Using estimates for geometric porosity, equation (5) may be used to calculate a tortuosity τ = 1.7 ± 0.6. Using the raw data for each experiment instead of the fitted D_F, the weighted mean and standard deviation of the diffusion coefficient for the high-pressure experiments is 0.49 ± 0.18 cm^2 s^{-1}. With the same value of $\mathcal{D}_{12}$ given above, the obstruction factor $D/\mathcal{D}_{12} = \phi/\tau$ is 0.18 ± 0.07 and the tortuosity factor is τ = 1.5 ± 0.6.

[104] Equation (5) is true for Fickian diffusion and is therefore appropriately applied to data taken at higher pressures. If this expression is used with values of D obtained at ~600 Pa, the value of the tortuosity obtained is τ = 2.4 ± 0.3. The result equation (5) (which is used for all other simulants for which variable pressure data were not

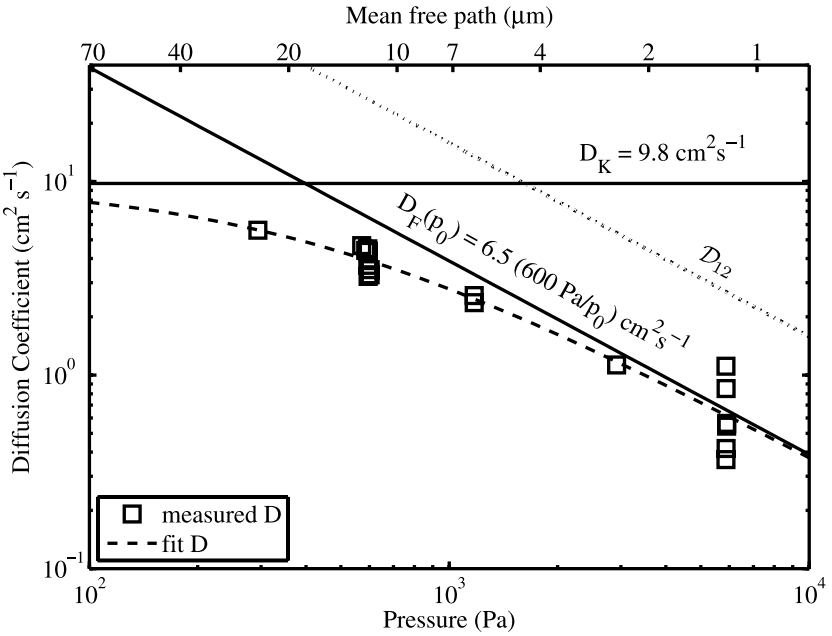

Figure 7. Diffusion coefficients versus pressure for 5 cm samples of 40–70 μm beads. Errors in D are smaller than the symbols. The diffusion coefficients obtained from equation (26) are plotted along with the fitted parameters $D_F(p_0)$ and D_K (solid lines) and their interpolation D (dashed line). $\mathcal{D}_{12}$ is the free-gas diffusion coefficient as given by the expression of *Wallace and Sagan* [1979] (dotted line).

available) is an overestimate of tortuosity since the 600 Pa data are in the transition regime (see Figure 7) and include a component of Knudsen diffusion.

[105] A distinction must be drawn between tortuosity and the tortuosity factor. As reviewed by *Epstein* [1989], "tortuosity" refers directly to the ratio of the pore path length L_e to the length of the porous medium along the major flow or diffusion axis L. However in calculating the effective diffusion coefficient using a parallel-pore conceptual model, a second factor of L_e/L enters the expression because of the increase in capillary velocity over the axial velocity (along L) when there is no divergence of the flow. Thus our factor of τ is the "tortuosity factor", equal to $(L_e/L)^2$. The methods using either high-pressure data or (equivalently) the fitted Fickian diffusion coefficient give an increase in pore path length oven sample length, L_e/L, of 1.3, while the overestimate made with individually determined values of D gives $L_e/L = 1.6$.

[106] At lower pressures, as diffusion begins to transition into the Knudsen regime, D ceases to depend on pressure through $\mathcal{D}_{12}$ and the obstruction factor must incorporate additional factors as shown in equations (12) and (13). In the formalism used by *Evans et al.* [1961], the τ in these equations is the same as the τ in equation (5). We can use equation (14) to determine that the value of τ above will correspond to our fitted value of $D_K = 9.8$ cm^2 s^{-1} if the value of $\bar{r}$ for glass beads is 14.4 μm. This is only slightly larger than the theoretical minimum pore space of 11.96 μm, suggesting that the sample is near closest-packing and that few pathways much larger than $\sim$40 μm are available for diffusion. Calculated obstruction factors ($D/\mathcal{D}_{12}$) for glass beads range between 0.12 and 0.23 except for two outliers at 0.35 and 0.46 measured at high pressures. The majority are within the range of obstruction factors given by *Currie* [1960] for closest packing (0.13) to cubic packing (0.38) of spherical particles.

[107] Mechanical packing (tamping, shaking, or pressing) of this sample does not measurably reduce porosity, and neither porosity nor tortuosity nor their ratio correlates strongly with mass loss rate (ϕ: R = -0.230, τ: R = 0.185, ϕ/τ: R = -0.245). These same quantities also do not correlate strongly with free-gas diffusion $\mathcal{D}_{12}$ (R = 0.050, -0.123, 0.077, respectively). The diffusion coefficient is poorly correlated with $\mathcal{D}_{12}$ (R = 0.232), and ϕ correlates poorly with τ (R = -0.222). There are no apparent correlations between quantities that should not be correlated, indicating that our method of extracting tortuosity is not systematically offset.

[108] The flux data show a greater spread in values for the thinner samples. A major factor which may contribute to the reduction in scatter with thickness is the averaging of pore geometry along the sample. The loose glass beads have a mean diameter of $\sim$55 μm. The measured obstruction factors suggest packing densities between hexagonally close-packed and cubic-packed, implying that there are between 180 and 230 layers of particles per centimeter. For thicker samples, the properties of the medium can average out and present smaller variations between experiments. Additionally, large voids occurring as a result of random packing will offer a very efficient path of vapor transport which could significantly impact the sample diffusivity. Such voids would be a smaller proportion of the total length for thicker samples, thus offering fewer wide, connected paths from the ice to the surface.

5.1.6. Water Contents

[109] Following each diffusion experiment, samples were weighed, baked in an oven at 110°C for >12 hours, and weighed again to gravimetrically determine water contents (per ASTM test method D2216). The weighing techniques employed allowed the determination of mass differences to within ±1 g. For 40–70 μm glass beads, the difference between pre- and post-bake masses was never more than this detection limit except for experiments with 10 cm samples. These large samples never exhibited more than 3 grams of difference, which corresponds to a maximum 6 mg/g of water content.

[110] At the end of experiments involving 5 and 10 cm sample columns, the bottom 2 cm of sample exhibited mild cohesion while the upper portions of the sample showed none. This suggests that the water content would be relatively higher at the base of the sample if it were measured independently. Such a non-uniform distribution of adsorbed water could reflect the vapor gradient along the sample length. A higher partial pressure near the bottom would cause a larger degree of adsorption there and some threshold water content for cohesion may be reached.

[111] The strongly linear behavior of the mass-loss curves following the initial thermal transients suggests that the absorptive capacity of the samples is filled in less than the transient time. This rate is much faster than would be obtained given only the ice retreat rates in the post-transient interval. It is likely that higher vapor pressures in thermal transient phase, vapor pumping during evacuation of the chamber, or absorption from the relatively moist freezer atmosphere acts to fill absorptive sites quickly. See the discussion of adsorption below (section 6.1) for more detail on the steady-state nature of these experiments.

5.1.7. Other Effects

[112] If the transition rate from ice into vapor is comparable to the diffusive flux, it will limit the flux measured. For a given ice temperature, the total flux would be independent of the sample thickness if the flux were sublimation rate limited. For such a constant flux, D would be observed to increase with sample thickness. This is observed in our uncorrected samples, though the effect may be due also to gas diffusion in the gaps. The correction term removes both effects simultaneously. Since $z_{corr} < z$, we know the sublimation limit correction is small, so our direct measurements of vapor density at the hygrometer, total flux, and our assumption of a saturated atmosphere below the sample is valid.

[113] Sublimation carries away the latent heat of the subliming ice (2845 kJ/kg at 0°C), cooling the sample surface. Multiple thermocouples embedded in the ice block during experiments both with and without a diffusive barrier show that temperature variations in the ice block are small. The maximum measured temperature difference across the 1 cm block (no cover, free ice) is no more than 0.8°C; the top surface near the caddy wall being the warmest spot. The ice (thermal conductivity: 2.2 W m^{-1} K^{-1}) therefore requires a heat input of approximately 180 W/m^2. Thermocouples near but not in contact with the a free ice surface record an atmospheric temperature of $\sim$255 K, which falls between that of the embedded thermocouples ($\sim$250 K) and

Table 4. Experimental Data and Diffusion Coefficients for Various Simulants[a]

Sample	Date	Δz, cm	p_0, Pa	T_{ice}, K	T_{air}, K	RH, %	J_1, mg m^{-2} s^{-1}	$\bar{c}$	$\Delta\rho_1$, g m^{-3}	D', cm^2 s^{-1}	$D/\mathcal{D}_{12}$
Frit 4	13 Feb	0.63	582	255.0	259.0	27.47	26.92	0.068	0.63	2.71 ± 0.55	0.10 ± 0.02
Frit 5	13 Feb	0.57	582	255.0	259.0	28.37	27.40	0.068	0.62	2.53 ± 0.55	0.10 ± 0.02
Frits 1 and 4	3 Feb	1.28	594	257.9	260.3	16.56	23.25	0.078	1.08	2.75 ± 0.33	0.10 ± 0.01
	23 Feb	1.28	588	256.0	260.2	19.15	21.10	0.069	0.83	3.26 ± 0.42	0.12 ± 0.02
	24 Feb	1.28	586	256.9	260.1	20.05	18.37	0.075	0.91	2.57 ± 0.21	0.10 ± 0.01
	28 Feb	1.28	584	256.8	259.9	21.09	21.34	0.075	0.89	3.07 ± 0.33	0.12 ± 0.02
	1 Mar	1.28	542	256.5	260.8	11.04	21.54	0.072	1.00	2.75 ± 0.40	0.10 ± 0.01
Frits 5 and 8	3 Feb	1.20	594	257.4	260.1	18.83	19.63	0.076	0.98	2.39 ± 0.31	0.09 ± 0.01
	23 Feb	1.20	588	256.8	260.0	22.93	22.73	0.076	0.86	3.17 ± 0.43	0.12 ± 0.02
	24 Feb	1.20	586	256.6	260.2	19.45	22.67	0.072	0.88	3.08 ± 0.41	0.12 ± 0.02
	28 Feb	1.20	584	256.3	259.8	22.74	22.12	0.073	0.82	3.25 ± 0.44	0.12 ± 0.02
	1 Mar	1.20	542	256.0	260.9	9.94	23.89	0.068	0.97	2.95 ± 0.36	0.10 ± 0.02
Frits 1–4	28 Jan	2.52	610	258.5	261.0	7.39	14.18	0.074	1.30	2.74 ± 0.25	0.11 ± 0.01
	29 Jan[b]	2.52	609	259.0	261.0	5.80	13.96	0.077	1.39	2.52 ± 0.22	0.10 ± 0.01
Frits 5–8	28 Jan	2.46	610	258.7	260.9	3.67	15.26	0.072	1.38	2.71 ± 0.24	0.11 ± 0.01
	29 Jan	2.46	609	258.8	260.9	7.28	15.58	0.077	1.34	2.85 ± 0.26	0.11 ± 0.01
	15 Feb	2.46	630	258.7	261.1	15.99	14.82	0.079	1.17	3.12 ± 0.31	0.13 ± 0.02
Frits 1–8	20 Mar	5.07	589	259.8	261.5	10.12	7.79	0.091	1.41	2.80 ± 0.24	0.11 ± 0.01
	21 Mar	5.07	589	259.8	261.6	10.01	7.98	0.091	1.42	2.85 ± 0.24	0.11 ± 0.01
JSC Mars-1	3 Apr	2.03	595	254.6	260.8	18.99	23.97	0.061	0.68	7.18 ± 0.90	0.27 ± 0.04
	22 Mar	5.05	594	257.9	261.2	13.55	11.58	0.077	1.11	5.29 ± 0.49	0.20 ± 0.02
	22 Mar	5.08	594	257.6	261.1	11.40	13.12	0.073	1.11	5.98 ± 0.54	0.23 ± 0.03
	3 Apr	10.11	608	259.0	261.4	7.98	6.29	0.079	1.34	4.73 ± 0.39	0.18 ± 0.02
1–3 μm loose	24 Oct	0.98	503	257.7	260.8	10.47	22.60	0.087	1.15	1.93 ± 0.26	0.06 ± 0.01
	17 Apr	2.09	584	255.8	260.7	17.91	17.45	0.067	0.81	4.50 ± 0.52	0.17 ± 0.02
	17 Apr	2.00	584	255.1	260.5	15.25	20.15	0.061	0.80	5.07 ± 0.57	0.19 ± 0.03
1–3 μm packed	2 Nov	0.95	547	260.3	261.3	10.53	12.10	0.105	1.48	0.77 ± 0.10	0.027 ± 0.005
	4 Nov	0.96	540	260.7	262.3	5.59	12.24	0.107	1.62	0.73 ± 0.09	0.025 ± 0.005
	25 Apr	1.04	604	261.2	259.2	11.93	8.69	0.101	1.63	0.55 ± 0.07	0.022 ± 0.003
	25 Apr	1.11	604	261.1	258.2	9.51	8.96	0.099	1.64	0.60 ± 0.07	0.024 ± 0.003
	14 Sep	2.07	625	261.4	262.7	6.98	1.65	0.099	1.70	0.20 ± 0.02	0.008 ± 0.001
	21 Apr	2.21	591	260.1	261.5	8.38	4.08	0.091	1.48	0.61 ± 0.06	0.023 ± 0.003
	21 Apr	2.20	591	259.8	261.3	7.45	9.29	0.088	1.46	1.40 ± 0.13	0.053 ± 0.006

[a]All experiments were carried out at −10°C under 600 Pa CO_2. Correction terms were either near zero (frits) or not determined due to insufficient data. Raw diffusion coefficients D' are reported.
[b]Experiment on 29 Jan with frits 1–4 was run upside-down to check for gravity-dependent effects.

the RTD temperature element in the hygrometer (~260 K). The apparent primary heat input to the ice is thus the warmer chamber atmosphere. When the ice is uncovered, this heat reaches it most effectively through convection. When a sample overlies the ice, heat is conducted through the diffusive barrier and the caddy walls. The ice temperature measured for 1 cm samples is 256.1 K, for 5 cm samples, 259.3 K, and for 10 cm samples, 260.1 K. The chamber atmosphere is 261 ± 0.6 K in all cases. This suggests that the thicker samples have heat inputs similar to the thin-sample cases, but their diffusive resistance allows less efficient cooling through sublimation.

5.2. The 40–70 μm Glass Beads at −20°C

[114] Data for this simulant are shown in Table 2. Several experiments have been run on the 40–70 μm beads at reduced temperatures. A walk-in freezer at a nominal temperature of −20°C houses the second vacuum chamber described in section 3.2.

[115] At lower temperatures the saturation vapor pressure over the ice is much smaller. As per equation (19), the advective contribution to the flux is therefore substantially lower. An insufficient number of data points and a small number of sample thicknesses prevent the calculation of a correction term. The data presented are the raw diffusion coefficients. The weighted mean and standard deviation of the diffusion coefficients is $D = 4.21 \pm 0.65$ cm^2 s^{-1}. This is slightly lower than the value determined for samples run at −10°C, but are indistinguishable within the range of systematic scatter. Extrapolation to 200 K results in $D = 3.03 \pm 0.47$ cm^2 s^{-1}, nearly identical to the extrapolation of the −10°C value of D. The difference in gas-gas diffusion between the −10°C and −20°C experiments is ~5%, being slightly lower in the colder case. The calculated tortuosity at −20°C, $\tau = 2.4 \pm 0.4$, is virtually identical to the −10°C case, and the obstruction factors are likewise similar.

5.3. Glass Frits

[116] Data for this simulant are shown in Table 4. To check the degree of systematic variation in our experimental setup, we performed a series of experiments with porous glass filter disks, or "frits". Stacks of frits with a nominal

pore size of 50–80 μm were assembled with electrical tape into columns of 1 to 8 frits ($\sim$0.5 to $\sim$5 cm) which were then fastened with tape onto caddies full of ice. The distance between the ice and the frits at the start of the experiments was less than 1 mm. The calculated porosity of the frits is 42 ± 2%.

[117] The calculated correction term z_{corr} was approximately zero and was therefore neglected; no correction was applied in the following analysis. The diffusion coefficient determined, 2.80 ± 0.22 cm^2 s^{-1}, is about a factor of 1.6 lower than that measured for the unconsolidated 40–70 μm beads. The measured porosities of the frits are indistinguishable from the value for glass beads. Hence the lower diffusivity can be attributed to a more tortuous geometry of the sintered glass frits. The calculated values of τ for the frits are 3.9 ± 0.4. This higher tortuosity may arise from the high temperatures and pressures of the sintering process; it is likely that some of the large pore spaces which could occur in randomly packed and unconsolidated material are eliminated.

[118] As expected, the porous frits exhibit a lower degree of systematic scatter compared with that in the data for unconsolidated media. The uncertainty in the diffusion coefficients for the frits is $\sim$6%, while that for the glass beads is $\sim$16%.

[119] To check that there were no gravity-dependent effects such as buoyancy, an inverted experiment was performed. Two sets of frits were run as usual for several hours. Then the chamber was opened and one set was inverted, with a physical gap which allowed free-gas flow at the sample surface. The difference between the two runs of the inverted sample was 1.9%, while the difference between the two runs of the unaltered set was 3.1%, showing that systematic differences in the experiment exceed any measurable gravity effect on mass loss. The expected gravity-dependent effect is small as discussed in section 2.6.

5.4. JSC Mars–1

[120] Data for this simulant are included in Table 4. JSC Mars–1 is the <1 mm fraction of weathered volcanic ash from the Pu'u Nene cinder cone, Hawai'i. The grains are composed of feldspar and Ti-magnetite, with minor olivine, pyroxene and glass, and have an average density of 1.91 ± 0.02 g cm^{-3}. The uncompacted porosity is reported as 54%, decreasable to 44% upon vibration [*Allen et al.*, 1997]. Much of the mass of JSC Mars–1 is in particles larger than 149 μm, but there is a significant fraction of particles smaller than 5 μm [*Allen et al.*, 1998]. See the micrograph in Figure 2 d for representative particle shapes. Compared to the 40–70 μm glass beads, Mars–1 has larger, more angular particles and a significant fraction of void-filling fines. However, the size and frequency of these fines is small and is not sufficient to block a significant fraction of the available pore space [*Allen et al.*, 1997].

[121] The measured porosity is 58 ± 2%, significantly larger than that determined for glass beads (44%). This is due to the highly angular nature of the JSC Mars–1 particles; the interlocking jagged edges allow a more inflated structure to be stable against compaction. The angular nature of these particles makes an estimation of the maximum and minimum pore sizes difficult. Pore spaces of approximately the same size as the largest particles would be rare because of infilling of larger interstices with smaller particles.

[122] Unlike all other simulants, the JSC Mars–1 exhibits a pronounced decrease in raw diffusion coefficients with thickness. This is opposite the expected trend which would arise from the effects discussed in section 4.2. We suspect that the wide grain size distribution permits significant packing effects which result in smaller true diffusivities for thicker samples. The weighted mean and standard deviation of measured diffusion coefficients for JSC Mars–1 is 5.36 ± 0.72 cm^2 s^{-1}. This is slightly larger than the corrected value for glass beads, but still falls within the range of uncertainties. The obstruction factor, 0.21 ± 0.03, is larger than the obstruction factor for glass beads, and the tortuosity τ = 2.6 ± 0.4 is slightly higher. Higher tortuosity is likely a consequence of the wider particle size distribution and angular particle shapes which give rise to a more convoluted flow geometry.

[123] A significant difference between the JSC Mars–1 and both glass beads and borosilicate frits is the amount of water retained during the course of an experiment. Approximately 10 g of water (69 mg/g) was retained at the end of a diffusion experiment with 5 cm of JSC Mars–1. JSC Mars–1 has a larger fraction of small particles than either of the two glass simulants. This higher available surface area may be able to hold onto a larger amount of water. Phyllosilicates, which could accommodate water in interlayer spaces, amount to less than 1% of the mass of the sample. More significant are small particles of weathered ash minerals including palagonite, glass, and nanophase ferric oxides which are abundant and contribute greatly to the specific surface area.

5.5. 1–3 Micron Dust

[124] Data for this simulant are shown in Table 4. The mean particle size of the Arizona dust is 1.19 μm with a standard deviation of only 0.49 μm. The dust easily forms weak mm to cm sized aggregates that may be broken up by sieving, although they reform upon settling or mechanical agitation. Pore sizes are therefore expected to be bimodal, with a peak at small sizes ($\sim$2 μm) occurring within the aggregates, and a second, broad peak for interaggregate pores at sizes much larger than in any of our other simulants ($\sim$1 mm) [*Yu et al.*, 2003]. Mechanical packing destroys the spaces between the aggregates and leaves only the smaller pores. Regardless of the distribution of pore space between large and small pores, the loose, aggregated material has a calculated geometric porosity of 88 ± 1%, while compressional packing results in a reduced porosity of 76 ± 2%.

[125] Data have not been taken at a sufficient spread of thicknesses to enable the calculation of a correction term for the 1–3 μm dust; the raw diffusion coefficients are reported. A significant difference is seen between loose and packed dust, the former being indistinguishable from the other simulants studied. The weighted mean and standard deviation of the diffusion coefficient for the loose dust is 2.81 ± 1.32 cm^2 s^{-1}; the error bars are within the range of 40–70 μm beads and the glass frits. Packed dust exhibits a much lower diffusivity. Packed samples of dust have a mean D of 0.38 ± 0.26 cm^2 s^{-1}, with one of the 2 cm thick experiments giving a diffusion coefficient of 0.20 cm^2 s^{-1}

Table 5. Summary of Results for the Experiments Carried Out at −10°C and 600 Pa in CO_2 Unless Otherwise Noted[a]

Sample	T_{ice}, K	D, $cm^2\ s^{-1}$	$D(200\ K) \propto T^{3/2}$, $cm^2\ s^{-1}$	$D(200\ K) \propto T^{1/2}$, $cm^2\ s^{-1}$	Porosity, %	$\mathcal{D}_{12}$, $cm^2\ s^{-1}$	$D/\mathcal{D}_{12}$	Tortuosity
40–70 μm beads	258.2 ± 1.7	4.49 ± 0.69[b]	3.06 ± 0.47	3.95 ± 0.61	44 ± 2	26.2 ± 2.2	0.17 ± 0.03	2.4 ± 0.3
40–70 μm beads, 6 kPa	261.2 ± 0.1	0.49 ± 0.18	0.33 ± 0.12	0.43 ± 0.16	42 ± 1	2.7 ± 0.2	0.18 ± 0.07	1.5 ± 0.6
40–70 μm beads, −20°C	249.4 ± 0.5	4.21 ± 0.65	3.03 ± 0.47	3.77 ± 0.58	44 ± 2	24.9 ± 2.1	0.17 ± 0.03	2.4 ± 0.4
40–70 μm beads, N_2	258.3 ± 1.9	5.33 ± 0.43[b]	3.63 ± 0.29	4.69 ± 0.38	43 ± 1	33.4 ± 2.1	0.16 ± 0.01	2.6 ± 0.2
"Coarse" glass frits	257.4 ± 1.5	2.80 ± 0.22	1.92 ± 0.15	2.47 ± 0.19	42 ± 2	26.4 ± 2.3	0.11 ± 0.01	3.9 ± 0.4
JSC Mars–1	257.3 ± 1.6	5.36 ± 0.72	3.67 ± 0.50	4.72 ± 0.64	58 ± 2	26.2 ± 1.8	0.21 ± 0.03	2.6 ± 0.4
1–3 μm dust: loose	256.2 ± 1.4	2.81 ± 1.32	1.94 ± 0.91	2.48 ± 1.17	88 ± 1	29.7 ± 1.7	0.09 ± 0.04	5.3 ± 1.9
1–3 μm dust: packed	260.6 ± 0.6	0.38 ± 0.26	0.25 ± 0.17	0.33 ± 0.23	76 ± 2	25.8 ± 0.9	—	12.1 ± 5.0[c]

[a]Weighted averages and standard deviations for T_{ice}, D, $\mathcal{D}_{12}$, $D/\mathcal{D}_{12}$ and tortuosity for all samples of a given type are listed. Diffusion coefficients are extrapolated to 200 K using $D \propto T^{3/2}$ and $D \propto T^{1/2}$ as appropriate for Fickian and Knudsen diffusion, respectively.
[b]Corrected D was reported for samples for which correction data was available.
[c]Tortuosity was estimated from the Knudsen diffusion coefficient and equation (14).

and another exhibiting 1.4 $cm^2\ s^{-1}$. The small number of measurements on dust and the presence of outliers results in formal standard deviations in D and τ which are large. Further measurements are needed to refine these results and reduce the uncertainties.

[126] A chamber pressure of 600 Pa places pores of micron size on the edge of the Knudsen regime, $r/\lambda_1 = 0.17$. The Knudsen obstruction factor is thus defined with a quantity K_0, which depends on other factors in addition to ϕ and τ. Equations (12), (13), and (14) may be used to calculate a value of τ for the dust particles, with a value of $\bar{r} = 2$ μm. Using this method, loose dust has $\tau = 5.0 \pm 1.7$, while the method used for other simulants (equation (5)) gives $\tau = 5.3 \pm 2.0$. This suggests that the loose dust behaves more like a coarser porous medium and is predominantly in the Fickian mode of diffusion. Packed dust, on the other hand, gives a tortuosity of 12.3 ± 5.1 with the Knudsen-appropriate equations, but $\tau = 23.5 \pm 10.9$ with equation (5). This estimate for τ is only as certain as the relationship between τ and D_K (equation (14)). While variable-pressure experiments were not performed on packed-dust to confirm that Knudsen diffusion was operating, the low values of diffusivity, differences between the two methods for calculating τ, and knowledge of particle size suggest that this is the appropriate regime. The small diffusivities and high tortuosities further suggest that a small layer of packed dust could dominate the diffusive resistance through a medium which is more open overall.

[127] The small particles of the Arizona dust retain water well. About half as much water as the JSC Mars–1, around 34 mg/g, was retained at the end of the experiments. The dust is nearly pure silica and has no special mineralogical means of binding the water. The retained water is likely held in place through capillary action and the large surface area of the dust and dust aggregates.

5.6. Summary

[128] Table 5 presents a summary of the data for each type of simulant. Mass fluxes for all samples are plotted versus sample thickness in Figure 8a. All simulants show decreas-

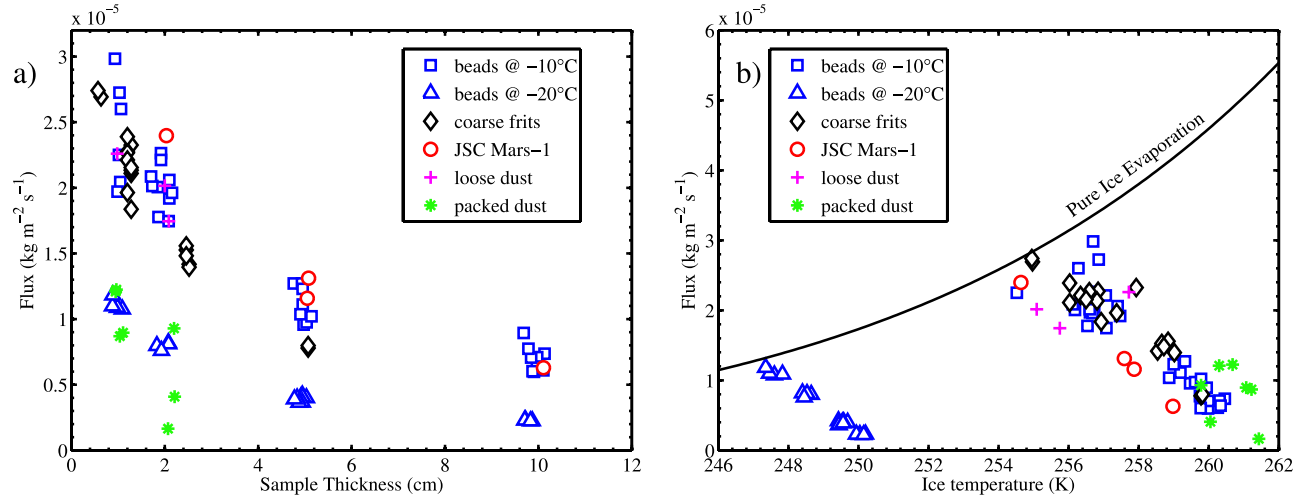

Figure 8. Flux versus (a) sample thicknesses and (b) temperature for each simulant as measured at 600 Pa and −10°C unless otherwise noted. Errors in flux are smaller than the symbols. In Figure 8a, the fluxes fall along the same curve for most experiments, notable exceptions being packed dust (asterisks) and −20°C experiments on glass beads (triangles). In Figure 8b, the measured fluxes all fall below the theoretical curve for evaporation of free ice calculated from *Ingersoll* [1970] for a dry atmosphere. Samples of larger thickness offer greater resistance to sublimation (and sublimation cooling) and thus exhibit lower fluxes and higher ice temperatures, resulting in the downward trend of flux with T_{ice}. The same trend occurs for more resistive packed dust versus loose dust (crosses).

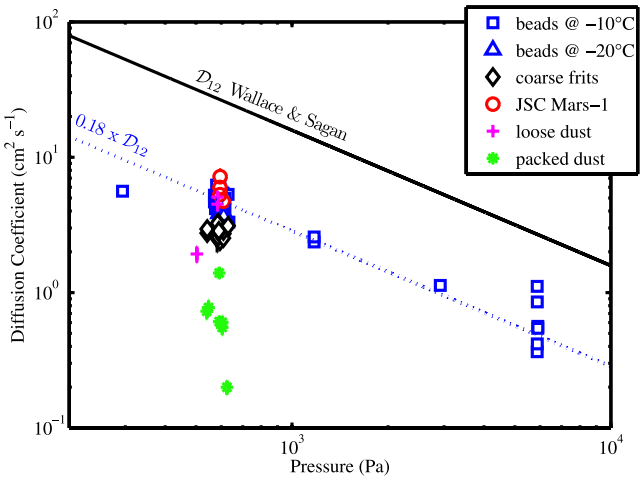

Figure 9. Diffusion coefficients versus pressure for all experiments. Errors in the diffusion coefficient are smaller than the symbols. The majority of experiments were run at 600 Pa. The solid line is the theoretically calculated value for the gas-gas diffusion coefficient $\mathcal{D}_{12}$ as given by *Wallace and Sagan* [1979] for $T = -10°C$. The dotted line shows $\mathcal{D}_{12}$ scaled by an obstruction factor of 0.18. Packed dust falls below the trend of other experiments but −20°C experiments do not.

ing flux at larger thicknesses. Experiments performed at −20°C, or experiments performed with packed dust, fall below the trend of other experiments. Figure 8b shows these fluxes as a function of temperature along with the evaporation rate curve for bare ice as given by *Ingersoll* [1970] for a dry atmosphere.

[129] We apply correction terms as per section 4.2 to experiments performed on glass beads at −10°C under CO_2 and N_2. The correction term determined for the glass frits is near zero and is neglected. Corrections are not applied to samples with an insufficient spread of thicknesses such as 1–3 μm dust and experiments on 40–70 μm glass beads at −20°C. A correction term is also not obtained for JSC Mars−1, which is a special case in which it is believed compaction effects result in different true diffusivities for different sample thickness.

[130] Figure 9 displays the data for all simulants taken at all pressures and at the temperatures measured (∼260 K or ∼250 K). The lines in Figure 9 represent extrapolated free-gas diffusion coefficients using the expression of Wallace and Sagan. The trend of the variable pressure data follows this line with a constant obstruction factor of ∼0.18. Diffusivities for all simulants measured at 600 Pa except for packed dust fall within the range of 2.0–6.2 cm^2 s^{-1}. The range of the mean values for different sample types and conditions (600 Pa only) is from 2.8 to 5.4 cm^2 s^{-1}. Packed 1–3 μm dust, which has values of D between 0.2–1.4 cm^2 s^{-1}, and a weighted mean value of 0.38 ± 0.26 cm^2 s^{-1}. The obstruction factor for most simulants is between 0.09 and 0.23, while for packed dust it is 0.008–0.053. This suggests that particle size and packing density, through their effect on the obstruction parameters ϕ and τ, are more important than particle shape (compare glass beads to frits), composition (compare glass simulants to JSC Mars−1), and size distribution (compare loose micron dust to other simulants).

[131] When extrapolated to the Mars-appropriate temperature of 200 K, the diffusion coefficients obtained for samples other than packed dust fall in the range of 1.9–4.8 cm^2 s^{-1}. Both this and the 260 K values are at the low end of the range of 0.4–13.6 cm^2 s^{-1} given by *Flasar and Goody* [1976].

[132] The tortuosity of the nondust samples exhibits a range from 1.5 to 3.9. The tortuosity determined for high-pressure samples is closest to the true value, determinations made with equation (5) being overestimates when the diffusion regime is in transition. For the loose dust, calculations of τ with either equation (14) or equation (5) give similar results. Dust, whether loose or packed, exhibits a higher porosity. Given the results of *Clifford and Hillel* [1986], who show that larger pore spaces accommodate a majority of the flux, loose dust with large interstices between aggregates behaves as if it were in the Fickian regime with $r/\lambda_1 \approx 100/12 = 8.3$. A significant difference (∼200%) results between the two calculation methods for τ when applied to the packed dust sample. Packed dust has only small pore spaces and its behavior is much closer to the Knudsen regime. Equation (14) provides a more appropriate description in this case and gives $\tau = 12.1 \pm 5.0$. The values of tortuosity as calculated for all samples are displayed graphically in Figure 10.

6. Discussion

[133] Our experimental setup simulates a static environment in which temperatures and humidities do not change

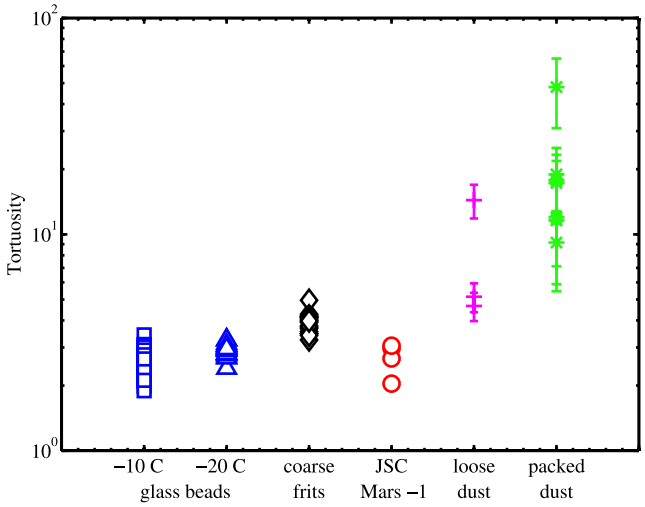

Figure 10. Tortuosities of the various simulants versus porosity. Errors for nondust samples are smaller than the symbols. Tortuosities for packed dust samples are calculated using equation (14). Values for all other simulants are obtained through equation (5). Most simulants cluster around $\tau = 2–5$, even the more porous JSC Mars−1. Loose dust exhibits a spread in tortuosity from 5 to 15 with wide error bars. Packed dust is very tortuous, with τ ranging from 9 to 48.

significantly with time. A planetary subsurface is subjected to temperature and humidity variations on a variety of timescales, from diurnal to obliquity-scale, which can affect the transport of water.

6.1. Adsorption

[134] Rapid fluctuations in temperature arising from diurnal insolation changes could affect diffusion rates inasmuch as adsorption acts as a source or sink of water vapor. The nonequilibrium adsorption or desorption of water can have a significant effect on the instantaneous vapor density, and therefore on gradients in vapor density. Adsorption typically increases with partial pressure and therefore inhibits diffusion compared with a nonadsorbing environment by attenuating local vapor density gradients.

[135] Adsorption results in a modification of the effective diffusion coefficient by a factor of $(1 + (1/\phi)\partial\alpha/\partial\rho_1)$, where ϕ is the porosity, α is the density of the adsorbed phase, and ρ_1 is the vapor density [*Schorghofer and Aharonson*, 2005, and references therein]. When $\partial\alpha/\partial\rho_1 = 0$, there is no adsorption. When $\partial\alpha/\partial\rho_1 = \infty$, there is complete adsorption of any additional water and $D = 0$. The term $\partial\alpha/\partial\rho_1$ for Mars temperatures is several orders of magnitude greater than unity according to *Zent and Quinn* [1995] and *Jakosky et al.* [1997].

[136] This modification to the diffusion coefficient only applies when the system is out of equilibrium, when the adsorptive layer is undersaturated with respect to the local temperature and pressure and water adsorbs to the grain surfaces. If the temperature and local vapor density remain constant, the quantity of adsorbed water does not change with time; there is no longer any net exchange between the vapor and the adsorbate. Hence, in an environment that is temporally isothermal and isobaric, the diffusion remains unaffected by the adsorption after each local point in the regolith has reached an equilibrium with the vapor. Thus, in our static experimental setup, adsorptive effects only occur in the initial moments of exposure of the ice to the soil, and they disappear by the time the thermal and diffusive transients have passed. In section 5.1.6 we discuss how absorptive saturation obtains very quickly in our experimental setup, being complete when the thermal transients have died out.

[137] The maximum temperature fluctuation experienced by the sample after initial transients occurs at its upper surface and will be no greater than the maximum air temperature fluctuations (±0.45 K). With a specific surface area for glass beads between 0.015 and 0.03 $m^2\ g^{-1}$, such a change corresponds to a change in adsorbed mass of less than 1 μ g cm^{-3} (using the empirical isotherm presented by *Zent and Quinn* [1997] for the data of *Fanale and Cannon* [1971, 1974]). With these conditions the influence of adsorption cycles in our experiment is negligible.

[138] On Mars, the scenario where adsorption has the greatest affect on the diffusion of vapor will be if adsorption proceeds from saturation to complete desiccation and back over each cycle. The skin depth of adsorption and desorption is less than the thermal skin depth [*Jakosky*, 1983].

[139] Adsorption on Mars greatly affects vapor density gradients on diurnal timescales, but long-term subsurface ice evolution depends on average gradients and adsorption has no accumulated effect [*Jakosky*, 1985; *Mellon and Jakosky*, 1993; *Schorghofer and Aharonson*, 2005]. Thus these static experimental results are applicable to long-term near-surface ice evolution on Mars.

6.2. Temperature Oscillations

[140] The surface of Mars experiences large diurnal and seasonal temperature variations. The mean diffusive flux from a buried ice layer can be calculated using mean annual vapor densities [*Schorghofer and Aharonson*, 2005]. The time averaged density gradient in equation (2) is the same as the gradient of the time averaged density, because the time integral and the spatial gradient can be interchanged. Neglecting the temperature dependence of the diffusion coefficient, one can then express the diffusive flux as $\langle J_1\rangle = -D\ \langle\partial\rho_1/\partial z\rangle = -D\partial\langle\rho_1\rangle\partial z$. Angle brackets indicate a time average.

[141] In the intervening layer between the ground ice and the atmosphere, frost and adsorbed water may form periodically. Unless stable throughout the year, this water will be lost again at a different time during the temperature cycle and has no accumulated effect. In the long-term, it contributes nothing to the net vapor flux.

[142] The mean vapor density gradient is simply $\partial\langle\rho_1\rangle/\partial z \approx \Delta\langle\rho_1\rangle/\Delta z$, where $\Delta\rho_1$ is the difference between the vapor density at the surface and at the subsurface ice, and Δz is the spatial separation between these two points. For all but the most rapid timescales, mean annual values of vapor density control the evolution of subsurface ice. Since mean annual values govern the net transport, our diffusion coefficients obtained from static experiments are applicable to the time varying conditions on Mars.

6.3. Ice Table Evolution

[143] Investigation by *Smoluchowski* [1968] of conditions which would permit long (10 Gyr) survival times for buried ice was motivated by the assumption that Mars' climate may have allowed ice to be deposited at low latitudes very early in its history, but has remained essentially unchanged from its current conditions for the past ~3.5 Gyr. To obtain such survival times in a completely dry atmosphere, his calculations assume extremely low porosities which lead to very low-diffusion coefficients.

[144] The water content of Mars' atmosphere is not zero; the current mean annual vapor pressure of water at the surface is ~0.13 Pascals [*Farmer and Doms*, 1979; *Smith*, 2002]. This small but nonzero quantity of atmospheric humidity introduces a frostpoint temperature of 198 K and thereby establishes an ice table equilibrium depth. The ice table will move until the mean annual vapor density above the ice is equal to the mean annual vapor density in the atmosphere and will thereafter be stationary until either its temperature changes or the atmosphere becomes more or less humid.

[145] The equilibrium position of the ice table is not determined by regolith diffusivity, but solely by subsurface temperature and atmospheric water content. If ice is found (through, for example, neutron spectroscopy, ground-penetrating radar, or trenching) to exist at a position away from the expected depth of equilibrium with respect to the current climate, it is possible that some transport-limiting process is slowing down the adjustment of the ice table.

[146] Smoluchowski's work was based on the additional assumption that Mars' climate has been static for most of its

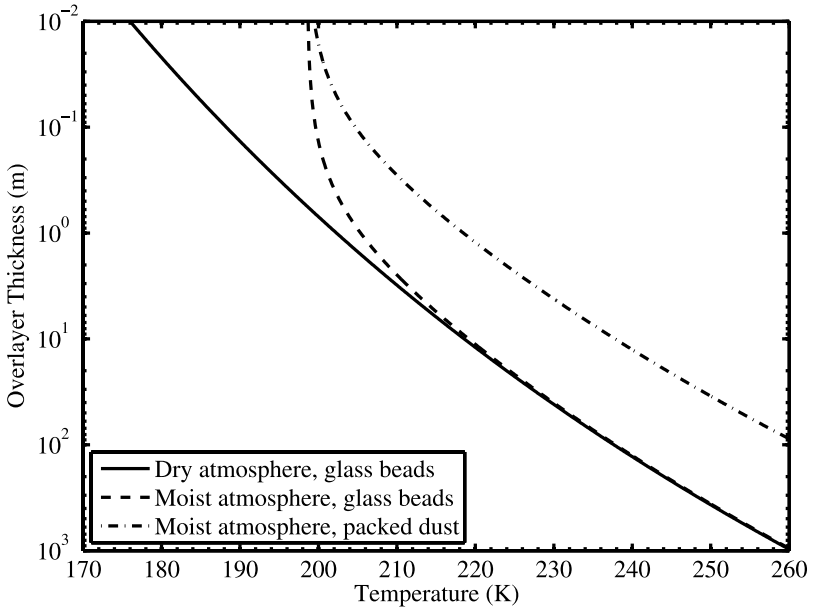

Figure 11. Regolith overlayer thickness required to allow one meter of ice retreat in ~38 kyr (one half of the 75 kyr climate cycle). The diffusion coefficients used are those extrapolated to 200 K via $D \propto T^{3/2}$ for glass beads and $D \propto T^{1/2}$ for packed dust, as appropriate for Fickian and Knudsen extrapolations, respectively. The values are in Table 5. The solid line represents zero atmospheric vapor density. The broken lines assume a present-day atmospheric vapor pressure of 0.13 Pa. With nonzero atmospheric humidity, ice is stable below the frostpoint and the overlayer thickness asymptotically approaches zero at this temperature (here 198 K).

history. More recent investigations (*Toon et al.* [1980] and many others since) have revealed that significant climatic variation occurs on more frequent timescales. Obliquity cycles of 125 kyr and 1.3 Myr and a longitude-of-perihelion precession with a 75 kyr period have dramatic effects on ice stability through the climatic variables of subsurface temperature and atmospheric water content [*Fanale et al.*, 1986; *Mellon and Jakosky*, 1995; *Zent and Quinn*, 1995]. Assuming climate conditions on Mars were similar to their current state beyond several hundred thousand years in the past is therefore unrealistic.

[147] The vapor transfer between the atmosphere and a buried ice-rich layer is $J = D\Delta\langle\rho_1\rangle/L$. The rate at which the ice table evolves toward its equilibrium depth in response to a change in climate depends, therefore, on the value of D, and also on the vapor density difference between the saturated vapor above the ice and the atmosphere $\Delta\rho_1$, the depth of burial L, and the thickness of ice added or removed Z (positive downward). These terms are related by the expression

$$-\frac{dZ}{dt} = -\frac{D\Delta\rho_1}{\rho_{ice}}\frac{1}{Z(t)}, \tag{31}$$

where ρ_{ice} is the density of bulk ice. For a dry regolith of thickness L overlying pure ice, the loss of an ice layer of thickness Z in time t is given by

$$Z(t) = \frac{D\Delta\rho_1}{\rho_{ice}L}t. \tag{32}$$

Assuming that subsurface ice can be recharged during more favorable times, a conservative estimate for the maximum lifetime of a buried ice layer during a period of desiccating climate may be calculated by equation (32).

[148] As an example, a 3% change in diffusivity at constant temperature would change the ice lost in one year by 3%. While diffusivity is a first-order control on the rate of subsurface ice evolution, its importance is dwarfed by the effects of subsurface ice temperature, particularly near the frostpoint. If the ice is near the frostpoint, a change by 5 degrees (less than 3%), from 200 to 205 K for example, will cause a 700% change in $\Delta\rho_1$. At higher temperature, a change of slightly less than 2%, from 260 to 265 K, will only change $\Delta\rho_1$ by 64%, but the absolute magnitude of the change will be much greater. In terms of ice loss, the former case means the difference between 3.6 and 24 mm of ice per year, while the latter is the difference between 34 and 22 m of ice per year.

[149] Consider the evolution of a layer of near-surface ice for ~38 kyr. This is one half-period of the shortest orbital climate variation (longitude-of-perihelion precession) and could represent the longest time during which the climate is in a single mode (e.g., ice loss) for some location on Mars. The depth of burial which would allow one meter of pure ice to retreat in this time by the method of equation (32) is presented in Figure 11 as a function of ice temperature.

[150] If the ice fills interconnected pore spaces of a structural regolith matrix with low-porosity ϕ, the removal of ice leaves behind a lag which increases in thickness. For a growing lag, L becomes Z(t) in (31) which makes t quadratic in Z. After integration, we obtain

$$Z(t) = \left[\frac{2D\Delta\rho_1}{\rho_{ice}}t + Z^2(0)\right]^{\frac{1}{2}}. \tag{33}$$

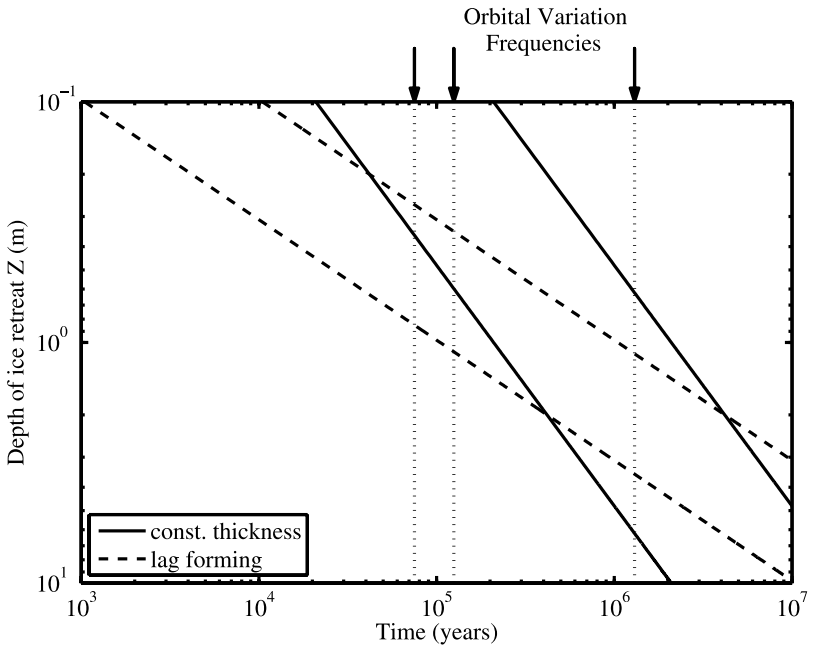

Figure 12. Retreat depth versus time for two values of the diffusion coefficient in a moist atmosphere. Solid lines show cases for pure ice under a regolith one meter thick. Dashed lines show lag-forming cases with an initial barrier of 1 mm. Values of D used are 3.0 cm^2 s^{-1} for the left lines, and 0.3 cm^2 s^{-1} for the right lines. T_{ice} = 200 K. Vertical dotted lines are, from left to right, the frequencies of 75, 125, and 1300 kyr climate cycles.

[151] The effect of the value of the diffusion coefficient on ice retreat depth versus time is shown in Figure 12 for ice at 200 K in a dry atmosphere for both "constant thickness" and "lag-forming" cases.

[152] Relatively large diffusion coefficients of around 3 cm^2 s^{-1} allow ice to respond quickly to a climate change. Within one half-period of the 75 kyr climate cycle, a pure ice table buried by one meter of dry regolith could retreat to a depth of 19 cm. A pore-filling ice table initially retreats at about the same rate because the area of ice exposed is reduced by the same factor ϕ as the volume density of ice, and would reach 60 cm in the same amount of time. A diffusion coefficient of 0.3 cm^2 s^{-1} causes the ice to respond more slowly and less than 1.9 cm of retreat is possible for a pure ice case in the same time. Warmer ice responds much more quickly. At 240 K, pure ice covered by 1 m of regolith with D = 0.3 cm^2 s^{-1} would retreat by more than 700 cm in 38 kyr.

[153] For the range of diffusivities measured in our experiments, the depth over which ice can respond to ~100 kyr climate cycles is less than approximately 1 m. This is similar to the difference in ice table equilibrium depths determined for a range of obliquities in the model of *Mellon and Jakosky* [1995]. Whether or not present-day subsurface ice has responded to recent climate variations and is at its equilibrium depth with respect to the current climate will depend both on the ice temperature, the diffusivity of the overlying regolith, and whether the ice is a pore-filling substance or is a solid slab of pure ice.

[154] For cases with very high ice filled porosity, for example, polar layered deposits where the material is likely to be only a few percent dust, a lower porosity lag will still form as the ice sublimes. This simple model is limited by the assumption of isothermal ice in equations (32) and (33) and Figure 12. As the ice front moves, its mean annual temperature will adjust to that specified by the soil thermal properties and the insolation at the surface. Soil thermal properties are very likely to be correlated with mass-transport diffusivity. Low-density materials with a small amount of interconnectivity between individual grains (such as dust) are likely to have low thermal conductivities and hence low thermal inertias.

6.4. Diffusion in Mars Surface Processes

[155] The degree to which the ice beneath a given regolith will be able to respond to variations of a particular frequency will depend on the value of the diffusion coefficient, lower values of D corresponding to a more sluggish response. Evidence for near-surface ice from Mars Odyssey [*Boynton et al.*, 2002; *Feldman et al.*, 2004] is consistent with climate model predictions which imply that the present-day Mars ice tables are at or near their equilibrium positions with respect to the present climate [*Mellon and Jakosky*, 1993; *Mellon et al.*, 2004; *Schorghofer and Aharonson*, 2005]. This suggests rapid communication between the subsurface ice and the atmosphere. Schorghofer and Aharonson estimate that a diffusivity of at least 1 cm^2 s^{-1} is required to achieve the observed balance between atmospheric water vapor and ground ice distribution within a single obliquity cycle. On timescales of years or decades, the coupling of atmospheric water circulation with the regolith will be strongest in soils with rapid diffusion. An upper limit on realistic soil diffusivities will set the maximum adjustment rate of subsurface ice to climate fluctuations.

[156] Likewise, the lowest realistic soil diffusivity sets the minimum adjustment rate of subsurface ice to climate fluctuations. With $D = 1$ cm^2 s^{-1} at 200 K and in a dry atmosphere, ice in the top meter can be sustained for at most 80 kyr. This result is obtained by inverting equation (33) for the time t it takes to retreat to depth Z, $t = (Z - Z_0)^2 \rho_{ice}/(2D\Delta\rho_1) \leq Z^2 \rho_{ice}/(2D\Delta\rho_1)$.

[157] The subsurface temperature cannot be expected to stay constant for longer than a few tens of thousands of years because of orbital variations in insolation. Variations on these longer timescales will be able to affect ice beneath porous regoliths with lower values of D. Long-term climate modeling should be sensitive to the distribution and extent of lower diffusivity regoliths. Additionally, during times of high atmospheric humidity the gradient in vapor density may either vanish, resulting in stable subsurface ice, or reverse, resulting in ice accumulation.

[158] Significant variability in the diffusive properties of the Martian regolith at different locations and depths is expected. The range of pore sizes and values of D given by the investigators mentioned in section 1.1 reflects this uncertainty. In the absence of any global-scale data on regolith porosities or other quantities that would enable the calculation of D, most existing models incorporate spatially homogeneous diffusion coefficients.

[159] Our results are important in light of the frequent use of diffusivity of regoliths as inputs to models. In their work considering the recent history of the northern polar layered deposits, *Levrard et al.* [2005] present as a possibility the "common presumption" than dust-containing polar water ice could form a thick lag deposit upon sublimation which would protect deeper ice. They introduce a factor f which reduces the flux when covered by a growing lag. This factor is directly related to the obstruction factor ϕ/τ; our values of ϕ/τ can inform estimations of the factor f.

[160] *Skorov et al.* [2001] claim that pore radii in Mars regoliths are between 0.1 and 10 microns and therefore Knudsen conditions obtain. In the same sentence, however, they say that sand- and granule- sized "clodlets" are present, which our experiments suggest would allow Fickian or near-Fickian transition diffusion.

[161] In papers considering conditions which could give rise to transient liquid water on present-day Mars, *Hecht* [2002], *Clow* [1987], and *Farmer* [1976] point out that the presence of a snow or dust cover can significantly suppress evaporative cooling. This circumvents the limitation identified by *Ingersoll* [1970] that evaporative cooling exceeds the solar constant already at temperatures below melting. The reduced heat loss allows ice in favorable environments to reach the melting point. The possibility of transient liquid applies both to the formation of geomorphic features such as crater-wall gullies and subglacial drainage networks, and also to problems of water availability for possible Martian organisms.

[162] Other investigators invoke low values of diffusivity as well. *Murray et al.* [2005] suggest that a near-surface barrier with a low-diffusion coefficient could explain geomorphic features in Cerberus Fossae as persistent equatorial ice rafts that have remained since the last eruption of water from Cerberus. *Head et al.* [2005] invoke low-diffusion coefficients to explain the possible existence of tropical glaciers on Mars. Appropriately for greater depths where porosity may be greatly reduced, *Krasnopolsky et al.* [2004] and *Weiss et al.* [2000] assume a small pore size of order microns when considering the diffusion of methane and other gases. These findings show high values of D for a range of unconsolidated regolith types, with lower values only appearing in mechanically modified soils.

6.5. Mars Regolith Properties

[163] The combined results of the experimental investigations and the calculations presented in this section are applicable to Mars only insofar as we can make reasonable estimates of true regolith properties. Dunes and other aeolian landforms indicate the widespread presence of particulate matter with sand-sized grains. Atmospheric scattering effects and observations by surface landers verify the global presence of very fine dust.

[164] The Mars Exploration Rovers (MER) both see soils composed of rounded grains with a maximum size of 100 μm. Grain sizes extend down to the limit of resolution of the Microscopic Imager, but the size distribution down to micron-size dust is not known. The soil compositions are remarkably uniform across the five landing sites of Viking, Pathfinder and MER, having more in common with each other than the analyzed rocks at those sites [*Yen et al.*, 2005]. Since aeolian processes are efficient at sorting grain sizes, it is possible that areas exist on Mars where the regolith is composed of windblown sand particles of nearly homogeneous size. Other areas may be dust laden and better represented by micron- or submicron-sized dust.

[165] *Putzig et al.* [2005] have used Thermal Emission Spectrometer (TES) observations of Martian surface thermal properties to estimate global thermal inertia at 3 km resolution. Along with earlier work by *Kieffer et al.* [1973] and *Christensen* [1986], these observations show that Mars' surface has large regions with a significant fraction of unconsolidated dust ($\leq$40 μm). Such materials are characterized by low thermal inertias, while both sand-sized particles and indurated fines can give intermediate values between loose dust and solid rocks. At 600 Pa, dust particles with diameters $\leq$2 μm will exhibit primarily Knudsen diffusion if the pore sizes are comparable to the grain size. Our results suggest that this condition only obtains when the dust has been packed by some mechanism. Regardless of how the dust is compacted, its thermal inertia will be higher than loose air-fall dust. Moderate thermal inertia regions indicative of a high proportion of sand-sized particles (approximated by the 40–70 μm beads) would fall in the transition region between Fickian and Knudsen diffusion.

[166] In their theoretical investigation of the effects of pore size distribution on subsurface ice survival, *Clifford and Hillel* [1983] calculated flux distributions through 12 model pore size distributions. Their results showed that in all cases of nonuniform pore size, the largest pores always accounted for the highest percentage of total flux. They thus concluded that the geometric factor which most significantly influences ground ice loss rates (other parameters like temperature and humidity being equal) is the porosity characterized by the larger ($\geq$1 μm in their simulants) pores. Real soils almost always have polydisperse grain sizes, and it is likely that aggregation operates on Mars as least as efficiently as it does on the Moon. If a soil has more than a few percent of its pore space accommodated by statistically larger pores, the diffusion will be dominated by these more open pathways. Despite

the presence of small pore spaces, the whole soil could have a diffusivity comparable to a monodisperse soil with an average pores size equal to its largest pores to within about 10–15% [*Clifford and Hillel*, 1983].

6.6. Obtaining Small *D* on Mars

[167] Our experiments indicate that, for a variety of simulants with a range of particle sizes, shapes, and pore space geometries, diffusivities under Martian surface conditions will be on the order of 2.8–5.4 $cm^2\ s^{-1}$, the obstruction factor being approximately 0.09–0.21. It is not easy to attain smaller values by packing well-sorted large grains; neither gravitational nor near-surface compressive packing will result in a substantial change in pore geometry. Evidence of dust deposition at lander sites and low thermal inertia values observed from orbit suggest a range of physical properties consistent with most real Martian sediments being porous and allowing significant diffusion of vapor [*Jakosky*, 1983]. The values of *D* given above are significantly higher than those invoked by some papers referenced in section 6.4.

[168] The shape of dust can affect its diffusive properties. Micron-size particles are not easily abraded and often exhibit angular forms whose irregular edges easily interlock and prevent more efficient packing arrangements. Even perfectly spherical particles may agglomerate because of electrostatic forces or by cohesion due to adsorption of water. Whether deposited as individual grains or as millimeter- to submillimeter-scale aggregates, the structure of air fall dust deposits is likely to be much more open than the physical packing limit, and the obstruction factor will likely be near the value of 0.18 observed for our loose dust samples.

[169] The simple idea of having wind-blown dust of the smallest particle sizes settle into the pore spaces of coarser exposed surface material, thereby blocking the escape of water vapor molecules, may not in fact produce the expected small effective diffusion coefficient. The results obtained here suggest that, in the absence of mechanical packing, the diffusion coefficient of the micron-sized particles is not very different from that of the larger particles.

[170] It is difficult to conceive of a purely mechanical process on Mars which could provide the packing force required to produce a significant reduction in the observed *D* (as was necessary for the laboratory measurements). Processes which result in systematically closer packing of the very fine particles, such as sedimentation or cementation, to produce a less porous layer (or the in-filling of the larger voids) form the basis of more plausible scenarios for the production of a vapor barrier than does simple wind-blown redistribution of the dust.

[171] Examples of processes which will produce low-diffusivity barriers with micron-size dust are as follows.

[172] 1. Caliche or duricrust may appear. Indurated soils, often described as ''duricrust,'' have been observed at Viking, Pathfinder, and MER landing sites. No conclusive observations of the chemistry of these crusts yet exist, but it is likely that cementation by mobile salts plays a role in their formation. Additionally, subsurface salts deposits have been observed at the MER Spirit landing site. Under certain conditions these could form subsurface cemented layers, similar to terrestrial caliche, which could impede the flow of water vapor.

[173] 2. Settling may occur in liquid water. Water can deflocculate dust aggregates, mitigate electrostatic repulsion, and lubricate the sliding of angular particles, all of which permit higher packing densities. In their paper where they consider Knudsen diffusion on Mars through mixtures of small ($\leq$10 μm) particles, *Clifford and Hillel* [1983] model their distributions after natural samples which have been sedimented in fluid and then dried. The MER rover Opportunity has discovered evidence for shallow standing water on Mars' surface at some point in the past [*Squyres et al.*, 2004]. Whether any dense layers of small particles formed at such times could have survived unbroken to the present is unknown, but seems unlikely. Additionally, dense layers formed in standing water have a tendency to crack upon drying, as observed on playas in terrestrial deserts and mud flats.

[174] 3. Physical packing may occur. This process, requiring a significant downward force, is unlikely to act over significant areas unless large-scale burial of a region acts to compact previously emplaced dust. This mechanism may operate in the formation and subsequent burial by fresh ice of polar layers. Exhumation processes may destroy whatever cohesive layers were formed, although still-buried dense layers of dust are possible. Additionally, mixtures of polydisperse grains which have less than a critical dust content (i.e., the quantity of fine dust required to fill the larger pore spaces) will not pack more tightly than is allowed by the larger grains.

[175] There are few investigations into the porous geometry of Martian air fall dust in the literature. *Moore* [1987] discusses the density and probable particle size composing ''drift material'' at Viking lander sites. A number of criteria suggest that the drift material examined by Moore is from 0.1–10 μm in size. The observed density of 1.0–1.3 $g\ cm^{-3}$ would, for basaltic material, correspond to a porosity of 44–66%. Such low porosities cannot be attained with our micron-sized dust without dispersal in water. The drift material may have been subject to some porosity-reducing surface process.

[176] Further studies are needed on the processes of dust deposition under Mars surface conditions so that pore size distributions for dust can be estimated for a wide range of particle sizes and shapes. On the basis of our current understanding of Mars soils and our laboratory observations, it seems difficult to produce low-diffusivity barriers, except perhaps by the action of liquid water. The process may be further enhanced by chemical deposition.

[177] Investigations on Mars processes that invoke low-diffusivity materials should address the formation mechanism of such barriers. Porous media with moderate diffusivities ($\sim$2–5 $cm^2\ s^{-1}$) are easily formed from a variety of regolith materials, but lower diffusivities are difficult to obtain even in the presence of micron-sized dust. Using the facility described above, we intend to investigate the effects of salt content, dust content in coarser-grained material, and thin dust layers on diffusive properties to help constrain the range of variability in diffusive barriers on Mars.

7. Conclusions

[178] We have measured diffusion coefficients in several regolith simulants under conditions of sublimation and at

pressures appropriate to the surface of Mars. The experimental setup used mimics the geometry and environment of Martian subsurface ice overlain by a porous material. Diffusion coefficients are obtained from mass loss, ice temperature, humidity, and sample thickness; we also measure simulant porosity and chamber pressure. Vapor transport theory is presented that is applicable not only to the experimental setup, but also to variable pressure and temperature environments as exist on Mars.

[179] Previous considerations of diffusive processes on Mars have been primarily based on the kinetic theory of gases in porous media or on experiments at conditions significantly different from those on the Martian surface. These studies suggest a wide range of possible values of the diffusion coefficient, from a high of 13.6 $cm^2\ s^{-1}$ to a low of 0.4 $cm^2\ s^{-1}$ for unconsolidated near-surface regoliths, with an extreme on the order of 10^{-3} $cm^2\ s^{-1}$ for extremely low-porosity materials.

[180] Our experiments with glass beads in the 40–70 μm size range are a proxy for aeolian sediments on Mars. Measured at a pressure of 600 Pa their diffusivity is $D = 4.49 \pm 0.69$ $cm^2\ s^{-1}$. The obstruction factor of 0.17 ± 0.03 and measured porosity of $44 \pm 2\%$ give a tortuosity of 2.4 ± 0.3. This value is significantly smaller than the value of $\tau = 5$ given by Smoluchowski (and quoted by subsequent investigators) for porosities around 50%.

[181] Data taken over a range of pressures and thicknesses provide a Fickian and a Knudsen diffusion coefficient for 40–70 μm glass beads. The pressure-dependent Fickian diffusivity is (600 Pa/p_0) $\times$ 6.5 $cm^2\ s^{-1}$ and the pressure-independent tortuosity in the Fick regime 1.8 ± 0.6. The Knudsen diffusivity is 9.8 $cm^2\ s^{-1}$. The crossover pressure where dominance changes between one regime and the other is found to be about 398 Pa. This is consistent with the definition of the transition region as given by the ratio of mean pore size to mean free path (r/λ_1). The highest experimentally measured diffusivity is 7.2 $cm^2\ s^{-1}$ for a thin sample of JSC Mars–1, which exhibits an obstruction factor of 0.27 ± 0.03.

[182] Measurements on a number of other simulants (porous fritted disks and loose 1–3 μm dust) give similar diffusivities to the glass beads. The values of diffusivity for each simulant are in Table 5. The range covered by these simulants is 2.8–5.4 $cm^2\ s^{-1}$. The only observation of a significantly reduced diffusivity is with mechanically packed 1–3 μm dust which exhibits an average D of 0.38 ± 0.26 $cm^2\ s^{-1}$. Diffusion coefficients are slightly reduced when extrapolated to 200 K using either the Fickian ($T^{3/2}$) and Knudsen ($T^{1/2}$) temperature dependencies (also in Table 5).

[183] Tortuosities (τ) are in the range of 1.8–5.3 for all simulants except the packed dust, for which higher values of $\tau = 12.3 \pm 5.1$ are calculated. Since the samples are measured at a pressure where the mean free path is not small compared to the mean grain size, the tortuosity and diffusion coefficients are suppressed by the Knudsen effect, especially for the packed dust which has the smallest pore sizes.

[184] The variation of D among experiments with the same simulant is 8 to 16% for nondust samples. We have shown, theoretically and experimentally, that gravity, adsorption, and other forms of diffusion play no significant role in the experiments.

[185] While the vapor density over ice as a function of temperature is a very strong determiner of the equilibrium position and evolution rate of subsurface ice, the diffusivity of the overlying regolith is also a first-order control on the rate of subsurface ice migration. In extreme cases, low-diffusivity barriers could act to protect buried ice from being lost during periods of dry climate as suggested by *Smoluchowski* [1968]. It is difficult to conceive of a purely mechanical process on Mars which could produce a significant reduction in porosity for micron-sized air fall dust and thereby obtain a diffusivity similar to Smoluchowski's low values. Invoking significant reduction of D requires an explanation of which processes lead to the formation of the low-diffusivity barrier and how those processes fit in context with other observations.

[186] There are a number of processes which may give rise to such barriers. The efficacy of such processes and their prevalence on past and present-day Mars warrant further study, particularly regarding particle-size effects and mixtures, and the ability of crusts of salt-cemented sediments to significantly reduce vapor diffusion.

Notation

a_w	water activity.
c	mass concentration of water vapor = ρ_1/ρ_0.
$\bar{c}$	average c across sample.
D	concentration diffusion coefficient for porous medium.
D_F	Fickian diffusion coefficient.
D_K	Knudsen diffusion coefficient.
D'	uncorrected ('raw') diffusion coefficient.
$\mathcal{D}_{11}$	coefficient of self-diffusion in free gas.
$\mathcal{D}_{12}$	concentration diffusion coefficient in free gas.
$\mathcal{D}_T$	thermodiffusion coefficient in free gas.
$\mathcal{D}_p$	barodiffusion coefficient in free gas.
d	particle diameter.
dT_{ice}	error in measured ice temperature.
J_1	mass flux of water vapor.
J_2	mass flux of carrier gas.
J_{Adv}	advective component of J_1.
J_{Diff}	diffusive component of J_1.
K_0	Knudsen regime structural parameter.
k	Boltzmann constant.
k_p	barodiffusion ratio.
k_T	thermodiffusion ratio.
L	dry regolith lag thickness or porous medium length.
L_e	pore path length.
M_1	molar weight of water.
M_2	molar weight of carrier gas.
m_1	molecular mass of water.
m_2	molecular mass of carrier gas.
n_0	total number density in gas phase, $n_0 = n_1 + n_2$.
n_1	number density of water vapor.
n_2	number density of carrier gas.
n_d	number density of particles in dusty gas model.
p_0	total pressure, $p_0 = p_1 + p_2$.
p_1	partial pressure of water.
p_2	partial pressure of carrier gas.
p_{ref}	reference pressure.
$p_{\mathrm{sv}}^{\mathrm{liq}}$	saturation vapor pressure over liquid water.

p_{sv}^{ice} saturation vapor pressure over ice.
R universal gas constant or correlation coefficient.
RH relative humidity.
r pore or particle radius.
$\bar{r}$ average radius.
T temperature.
T_{ice} temperature of ice surface.
T_{air} temperature of chamber air measured at hygrometer.
t time.
V_1 molecular volume of water.
V_2 molecular volume of carrier gas.
$\bar{v}_1$ mean velocity of H_2O molecules.
w vertical velocity of gas.
Z thickness of ice added or removed.
Z_0 initial ice table depth.
z depth.
z_{corr} correction term.
α density of adsorbed phase.
$\Delta\rho_1$ water vapor density difference.
Δz sample thickness.
κ intrinsic permeability of a porous medium.
λ_1 mean free path of water vapor.
μ dynamic viscosity.
$\pi\sigma_{12}^2$ scattering cross section.
ρ_0 total mass density, $\rho_0 = \rho_1 + \rho_2$.
ρ_1 density of water vapor.
ρ_{1A} density of water vapor at ice surface.
ρ_{1B} density of water vapor at lower sample surface.
ρ_{1C} density of water vapor at upper sample surface.
ρ_{1D} density of water vapor at hygrometer.
ρ_2 density of carrier gas.
ρ_{ice} density of ice.
σ_1 molecular radius of water.
σ_2 molecular radius of carrier gas.
τ tortuosity factor.
ϕ porosity.
Ω_{12} collision integral.

[187] **Acknowledgments.** We wish to thank Matt Siegler for his work on initial chamber development, and Steve Clifford and Bill Boynton for their helpful reviews. Early work was carried out at the Extraterrestrial Materials Simulation Laboratory (EMSiL) at JPL with the help of Jackie Green, Stephen Fuerstenau, and Greg Peters. This work was funded in part by the JPL Director's Discretionary Fund and by NASA's Mars Fundamental Research Program.

References

Allen, C. C., R. V. Morris, D. J. Lindstrom, M. M. Lindstrom, and J. P. Lockwood (1997), JSC Mars-1: Martian regolith simulant, *Lunar Planet. Sci.*, *282*, abstract 1797.

Allen, C., K. Jager, R. Morris, D. Lindstrom, M. Lindstrom, and J. Lockwood (1998), Martian soil simulant available for scientific, educational study, *EOS Trans. AGU*, *79*(34), 405–409.

Anderson, P. (1995), Mechanism for the behavior of hydroactive materials used in humidity sensors, *J. Atmos. Oceanic Technol.*, *12*, 662–667.

Arvidson, R., J. Gooding, and H. Moore (1989), The Martian surface as imaged, sampled, and analyzed by the Viking landers, *Rev. Geophys.*, *27*, 39–60.

Bose, N., and B. Chakraborty (1955–1956), Diffusion coefficients of vapours into pure gases and their mixtures, *Trans. Indian Inst. Chem. Eng.*, *8*, 67.

Boynton, W., et al. (2002), Distribution of hydrogen in the near-surface of Mars: Evidence for subsurface ice deposits, *Science*, *297*(5578), 81–85, doi:10.1126/science.1073722.

Carr, M. (1996), *Water on Mars*, 229 pp., Oxford Univ. Press, New York.

Chapman, S., and T. Cowling (1970), *The Mathematical Theory of Non-Uniform Gases*, 3rd ed., Cambridge Univ. Press, New York.

Christensen, P. (1986), Regional dust deposits on Mars: Physical properties, age, and history, *J. Geophys. Res.*, *91*(B3), 3533–3545.

Clifford, S., and D. Hillel (1983), The stability of ground ice in the equatorial region of Mars, *J. Geophys. Res.*, *88*(B3), 2456–2474.

Clifford, S., and D. Hillel (1986), Knudsen diffusion: The effect of small pore size and low gas pressure on gaseous transport in soil, *Soil Sci.*, *141*, 289–297.

Clow, G. (1987), Generation of liquid water on Mars through melting of a dusty snowpack, *Icarus*, *72*, 95–127.

Cooper, C., and J. Mustard (2002), Spectroscopy of loose and cemented sulfate-bearing soils: Implications for duricrust on Mars, *Icarus*, *158*, 42–55.

Crider, W. (1956), The use of diffusion coefficients in the measurement of vapor pressure, *J. Am. Chem. Soc.*, *78*, 924–925.

Cunningham, R., and R. Williams (1980), *Diffusion in Gases and Porous Media*, Plenum, New York.

Currie, J. (1960), Gaseous diffusion in porous media, part I: Dry granular materials, *Brit. J. Appl. Phys.*, *11*, 318–324.

deWiest, R. (1969), *Flow Through Porous Media*, Academic, New York.

Epstein, N. (1989), On tortuosity and the tortuosity factor in flow and diffusion through porous media, *Chem. Eng. Sci.*, *44*(3), 777–779.

Evans, R., G. M. Watson, and E. A. Mason (1961), Gaseous diffusion in porous media at uniform pressure, *J. Chem. Phys.*, *35*(6), 2076–2083.

Fanale, F., and W. Cannon (1971), Adsorption on Martian regolith, *Nature*, *230*, 502–504.

Fanale, F., and W. Cannon (1974), Exchange of adsorbed H_2O and CO_2 between the regolith and atmosphere of Mars caused by changes in surface insolation, *J. Geophys. Res.*, *79*(24), 3397–3402.

Fanale, F., J. Salvail, A. Zent, and S. Postawko (1986), Global distribution and migration of subsurface ice on Mars, *Icarus*, *67*, 1–18.

Farmer, C. (1976), Liquid water on Mars, *Icarus*, *28*, 279–289.

Farmer, C., and P. Doms (1979), Global seasonal variation of water vapor on Mars and the implications for permafrost, *J. Geophys. Res.*, *84*(B6), 2881–2888.

Feldman, W., et al. (2004), The global distribution of near-surface hydrogen on Mars, *J. Geophys. Res.*, *109*, E09006, doi:10.1029/2003JE002160.

Flasar, F., and R. Goody (1976), Diurnal behavior of water on Mars, *Planet. Space Sci.*, *24*(2), 161–181.

Freeze, R., and J. Cheng (1979), *Groundwater*, Prentice-Hall, Upper Saddle River, N. J.

Gilliland, E., R. Baddour, G. Perkinson, and K. J. Sladek (1974), Diffusion on surfaces. I. Effect of concentration on the diffusivity of physically adsorbed gases, *Ind. Eng. Chem. Fundam.*, *13*(2), 95–100.

Gilmore, M., M. Merrill, and R. Castano (2004), Effect of Mars analogue dust deposition on the automated detection of calcite in visible/near-infrared spectra, *Icarus*, *172*(2), 641–646, doi:10.1016/j.icarus.2004.08.009.

Greeley, R., R. Leach, B. White, J. Iversen, and J. Pollack (1980), Threshold windspeeds for sand on Mars: Wind tunnel simulations, *Geophys. Res. Lett.*, *7*(2), 121–124.

Grew, K., and T. Ibbs (1952), *Thermal Diffusion in Gases*, Cambridge Univ. Press, New York.

Gross, F., S. Grek, C. I. Calle, and R. U. Lee (2001), JSC Mars-1 Martian regolith simulant particle charging experiments in a low pressure environment, *J. Electrostat.*, *53*(4), 257–266.

Guglielmo, G. (1882), Sulla determinazione del coefficiente di diffusione del vapor acqueo per nell'aria, nell'idrogeno e nell'acido carbonico, *Ann. Phys. Chem.*, *6*, 475–477.

Hardy, B. (Ed.) (1998), ITS-90 formulations for vapor pressure, frostpoint, temperature dewpoint temperature, and enhancement factors in the range −100 to +100C, report, Natl. Phys. Lab., London.

Hare, D., and C. Sorensen (1987), The density of supercooled water. II: Bulk samples cooled to the homogeneous nucleation limit, *J. Chem. Phys.*, *87*(8), 4840–4845.

Head, J., et al. (2005), Tropical to mid-latitude snow and ice accumulation, flow and glaciation on Mars, *Nature*, *434*, 346–351, doi:10.1038/nature03359.

Hecht, M. (2002), Metastability of liquid water on Mars, *Icarus*, *156*, 373–386.

Hindmarsh, R., Van der Wateren, and A. Verbers (1998), Sublimation of ice through sediment in Beacon Valley, Antarctica, *Geogr. Ann., Ser. A*, *80*(3–4), 209–219.

Hippenmeyer, B. (1949), Die diffusion von wasserdampf in wasserstoff, stickstoff und deren gemischen, *Z. Angew. Phys.*, *1*, 549–557.

Holman, J. (1997), *Heat Transfer*, 8th ed., 696 pp., McGraw-Hill, New York.

Ingersoll, A. P. (1970), Mars: Occurrence of liquid water, *Science*, *168*, 972–973.

Jakosky, B. (1983), The role of seasonal reservoirs in the Mars water cycle. 1. Seasonal exchange of water with the regolith, *Icarus*, *55*, 1–18.

Jakosky, B. (1985), The seasonal water cyle on Mars, *Space Sci. Rev.*, *41*, 131–200.
Jakosky, B., A. Zent, and R. Zurek (1997), The Mars water cycle: Determining the role of exchange with the regolith, *Icarus*, *130*, 87–95.
Kennard, E. (1938), *Kinetic Theory of Gases*, McGraw-Hill, New York.
Kieffer, H., J. Chase, E. Miner, G. Münch, and G. Neugebauer (1973), Preliminary report on infrared radiometric measurements from Mariner 9 spacecraft, *J. Geophys. Res.*, *78*(20), 4291–4312.
Koop, T. (2002), The water activity of aqueous solutions in equilibrium with ice, *Bull. Chem. Soc. Jpn.*, *75*(12), 2587–2588, doi:10.1246/bcsj.75.2587.
Krasnopolsky, V., J. Maillard, and T. Owen (2004), Detection of methane in the Martian atmosphere: Evidence for life?, *Icarus*, *172*(2), 537–547, doi:10.1016/j.icarus.2004.07.004.
Landau, L., and E. Lifshitz (1987), *Fluid Mechanics*, Pergamon, Oxford.
Levrard, B., F. Forget, J. Laskar, and F. Montmessin (2005), A GCM recent history of northern Martian polar layered deposits: Contribution from past equatorial ice reservoirs, *Lunar Planet. Sci.*, *XXXVI*, abstract 1783.
Lide, D. (Ed.) (2003), *CRC Handbook of Chemistry and Physics*, 84th ed., CRC Press, Boca Raton, Fla.
Marrero, T., and E. Mason (1972), Gaseous diffusion coefficients, *J. Phys. Chem. Ref. Data*, *1*(1), 3–118.
Mason, E., and A. Malinauskas (1983), *Gas Transport in Porous Media: The Dusty-Gas Model*, *Chem. Eng. Monogr.*, vol. 17, Elsevier, Amsterdam.
Mellon, M., and B. Jakosky (1993), Geographic variations in the thermal and diffusive stability of ground ice on Mars, *J. Geophys. Res.*, *98*(E2), 3345–3364.
Mellon, M., and B. Jakosky (1995), The distribution and behavior of Martian ground ice during past and present epochs, *J. Geophys. Res.*, *100*(E6), 11,781–11,799.
Mellon, M., W. Feldman, and T. Prettyman (2004), The presence and stability of ground ice in the southern hemisphere of Mars, *Icarus*, *169*, 324–340, doi:10.1016/j.icarus.2003.10.022.
Moore, H. (1987), Physical properties of the surface materials at the Viking landing sites on Mars, *U.S. Geol. Surv. Prof. Pap.*, *1389*, 222 pp.
Moore, H., C. Spitzer, K. Bradford, P. Cates, R. Hutton, and R. W. Shorthill (1979), Sample fields of the Viking landers, physical properties, and aeolian processes, *J. Geophys. Res.*, *84*(B12), 8365–8384.
Murray, J., et al. (2005), Evidence from the Mars Express High Resolution Stereo Camera for a frozen sea close to Mars' equator, *Nature*, *434*, 352–356, doi:10.1038/nature03379.
Nagata, I., and T. Hasegawa (1970), Gaseous diffusion coefficients, *J. Chem. Eng. Jpn.*, *3*(2), 143–145.
Nelson, E. (1956), The measurement of vapour diffusivities in coal-gas and some common gases, *J. Appl. Chem.*, *6*, 286–292.
Neufeld, P., A. Janzen, and R. Aziz (1972), Empirical equations to calculate 16 of transport collision integrals $\Omega(l, s)^*$ for the Lenndard-Jones (12-6) potential, *J. Chem. Phys.*, *57*(3), 1100–1102.
O'Connell, J., M. Gillespie, W. Krostek, and J. Prausnitz (1969), Diffusivities of water in nonpolar gases, *J. Phys. Chem.*, *73*(6), 2000–2004.
Papendick, R., and J. Runkles (1965), Transient-state oxygen diffusion in soil: I. The case when rate of oxygen consumption is constant, *Soil Sci.*, *100*, 251–261.
Pollard, W., and R. Present (1948), On gaseous self-diffuson in long capillary tubes, *Phys. Rev.*, *73*, 762–774.
Putzig, N., M. Mellon, K. Kretke, and R. Arvidson (2005), Global thermal inertia and surface properties of Mars from the MGS mapping mission, *Icarus*, *173*, 325–341.
Reid, R., J. Prausnitz, and B. Poling (1987), *The Properties of Gases and Liquids*, 4th ed., McGraw-Hill, New York.
Rossie, K. (1953), Die diffusion von wasserdampf in luft bei temperaturen bis 300°c, *Forsch. Gebiete Ingenieurwes*, *19A*, 49–58.
Schorghofer, N., and A. Aharonson (2005), Stability and exchange of subsurface ice on Mars, *J. Geophys. Res.*, *110*, E05003, doi:10.1029/2004JE002350.
Schwertz, F., and J. Brow (1951), Diffusivity of water vapor in some common gases, *J. Chem. Phys.*, *19*(5), 640–646.
Skorov, Y., W. Markiewicz, A. Basilevsky, and H. Keller (2001), Stability of water ice under a porous nonvolatile layer: Implications to the south polar layered deposits of Mars, *Planet. Space Sci.*, *49*(1), 59–63, doi:10.1016/S0032-0633(00)00121-5.
Smith, M. (2002), The annual cycle of water vapor on Mars as observed by the Thermal Emission Spectrometer, *J. Geophys. Res.*, *107*(E11), 5115, doi:10.1029/2001JE001522.
Smoluchowski, R. (1968), Mars: Retention of ice, *Science*, *159*, 1348–1350.
Squyres, S., et al. (2004), The Opportunity Rover's Athena science investigation at Meridiani Planum, Mars, *Science*, *306*(5702), 1698–1703, doi:10.1126/science.1106171.
Sugden, D., D. Marchant, N. Potter, R. Souchez, G. Denton, C. Swisher, and J. Tison (1995), Preservation of Miocene glacier ice in East Antarctica, *Nature*, *376*, 412–414.
Toon, O., J. Pollack, W. Ward, J. Burns, and K. Bilski (1980), The astronomical theory of climatic change on Mars, *Icarus*, *44*, 552–607.
Trautz, M., and W. Müller (1935a), Die reibung, wärmeleitung und diffusion in gasmischungen XXXIII. die korrektion der bisher mit der verdampfungsmethode gemessenen diffusionskonstanten, *Ann. Phys.*, *414*(4), 333–352.
Trautz, M., and W. Müller (1935b), Die reibung, wärmeleitung und diffusion in gasmischungen XXXIV. neue messungen von diffusionskonstanten und abschliessende zusammenfaung über gas-diffusionskonstanten, *Ann. Phys.*, *414*(2), 353–374.
Wallace, D., and C. Sagan (1979), Evaporation of ice in planetary atmospheres: Ice-covered rivers on Mars, *Icarus*, *39*, 385–400.
Washburn, E., et al. (Eds.) (2003), *International Critical Tables of Numerical Data, Physics, Chemistry and Technology* [CD-ROM], 1st electron. ed., Knovel, Norwich, New York.
Weiss, B., Y. Yung, and K. Nealson (2000), Atmospheric energy for subsurface life on Mars?, *Proc. Natl. Acad. Sci. U. S. A.*, *972*(4), 1395–1399.
Winkelmann, A. (1884a), Ueber die diffusion von gasen und dämpfen I, *Ann. Phys. Chem.*, *258*(5), 1–31.
Winkelmann, A. (1884b), Ueber die diffusion von gasen und dämpfen II, *Ann. Phys. Chem.*, *258*(6), 152–161.
Winkelmann, A. (1889), Ueber den einfluss der temperatur auf die verdampfung und auf die diffusion von dämpfen, *Ann. Phys. Chem.*, *272*(1), 93–114.
Yen, A., et al. (2005), An integrated view of the chemistry and mineralogy of Martian soils, *Nature*, *436*, 49–54, doi:10.1038/nature03637.
Yu, B., J. Li, Z. Li, and M. Zou (2003), Permeabilities of unsaturated fractal porous media, *Int. J. Multiphase Flow*, *29*, 1625–1642, doi:10.1016/S0301-9322 (03)00140-X.
Zent, A., and R. Quinn (1995), Simultaneous adsorption of CO_2 and H_2O under Mars-like conditions and appliation to the evolution of the Martian climate, *J. Geophys. Res.*, *100*(E3), 5341–5349.
Zent, A., and R. Quinn (1997), Measurement of H_2O adsorption under Mars-like conditions: Effects of adsorbent heterogeneity, *J. Geophys. Res.*, *102*(E4), 9085–9095.
Zent, A., F. Fanale, J. Salvail, and S. Postawko (1986), Distribution and state of H_2O in the high-latitude shallow subsurface of Mars, *Icarus*, *67*, 19–36.

O. Aharonson and T. Hudson, Division of Geological and Planetary Sciences, California Institute of Technology, Pasadena, CA 91125, USA. (thudson@gps.caltech.edu)

N. T. Bridges, C. B. Farmer, and M. H. Hecht, Jet Propulsion Laboratory, California Institute of Technology, Pasadena, CA 91125, USA.

N. Schorghofer, Institute for Astronomy, University of Hawaii, 2680 Woodlawn Drive, Honolulu, HI 96822, USA.